

Research Aircraft Observations and Numerical Simulations of a Warm Front Approaching Vancouver Island

JAMES D. DOYLE

Naval Research Laboratory, Monterey, California

NICHOLAS A. BOND

University of Washington/JISAO, Seattle, Washington

(Manuscript received 9 September 1999, in final form 18 September 2000)

ABSTRACT

The mesoscale structure of the low-level flow and the character of the turbulence are investigated for a warm front as it approached the prominent terrain of the Pacific Northwest in the vicinity of Vancouver Island. Flight-level and airborne Doppler radar measurements collected from a National Oceanic and Atmospheric Administration P-3 research aircraft on 9 December 1995 during the Coastal Observation and Simulation with Topography experiment and high-resolution numerical simulations, performed with the Naval Research Laboratory's non-hydrostatic Coupled Ocean–Atmosphere Mesoscale Prediction System (COAMPS) model, have been used to document the warm front as it approached the coast and the structure of cool air trapped along Vancouver Island. This air mass was capped by a flat, thin transition zone of enhanced static stability and vertical wind shear. The flow within the trapped air mass was oriented parallel to the terrain of Vancouver Island, but appears to have been more an outflow from the Strait of Juan de Fuca than a barrier jet. Model sensitivity experiments suggest that the cold air that exited from the strait and the steep topography of Vancouver Island acted in concert to impede the northward movement of the front and steepen it near the surface. A wind speed maximum near the exit of the Strait of Juan de Fuca was consistent with transcritical expansion fan behavior. Both the observations from the gust probe system on the P-3, and output from COAMPS, indicate that the turbulent kinetic energy at low levels was relatively weak in the warm sector, moderate in the frontal zone, and strongest in the trapped flow near Vancouver Island.

1. Introduction

Coastal terrain can cause significant and not fully understood modifications to landfalling fronts and other storm phenomena. An opportunity to examine the detailed structure and evolution of these phenomena in the coastal zone was provided by the Coastal Observation and Simulation with Topography (COAST) experiment (Bond et al. 1997), which incorporated National Oceanic and Atmospheric Administration (NOAA) WP-3D research aircraft observations and high-resolution numerical weather simulations in a number of detailed case studies. A variety of synoptic situations have been investigated in the vicinity of the prominent terrain along the Pacific Northwest coast, namely, quasi-steady southwesterly flow impinging on Vancouver Island (Overland and Bond 1995) and the Olympic Mountains (Colle and

Mass 1996), and cold fronts in the vicinity of the Olympic Mountains (Colle et al. 1999), and in the nearshore (Braun et al. 1997) and coastal region (Yu and Smull 2000) of southern Oregon.

The structure and dynamics of atmospheric fronts during landfall are often complicated due to the diverse nature of the forcing in the coastal zone, which may include steep topography, strong surface flux gradients in the horizontal, and complex air–sea–land interaction (e.g., Rotunno et al. 1992; Rogers 1995). For example, Bjerknes and Solberg (1921) established an early conceptualization that illustrates the potential importance of steep coastal topography for the deformation and blocking of fronts near central Norway. In this study research aircraft observations taken during COAST are used to document a warm front during landfall near steep coastal orography. The research aircraft data are insufficient, however, to provide a complete depiction of the temporal and spatial evolution of the warm front during landfall. Numerical simulations are used to augment the observational analysis and to further explore the structure and dynamics of the landfalling warm front. One motivating factor for this study is that land-

Corresponding author address: James D. Doyle, Naval Research Laboratory, Marine Meteorology Division, 7 Grace Hopper Avenue, Monterey, CA 93943-5502.
E-mail: doyle@nrlmry.navy.mil

Report Documentation Page				Form Approved OMB No. 0704-0188	
Public reporting burden for the collection of information is estimated to average 1 hour per response, including the time for reviewing instructions, searching existing data sources, gathering and maintaining the data needed, and completing and reviewing the collection of information. Send comments regarding this burden estimate or any other aspect of this collection of information, including suggestions for reducing this burden, to Washington Headquarters Services, Directorate for Information Operations and Reports, 1215 Jefferson Davis Highway, Suite 1204, Arlington VA 22202-4302. Respondents should be aware that notwithstanding any other provision of law, no person shall be subject to a penalty for failing to comply with a collection of information if it does not display a currently valid OMB control number.					
1. REPORT DATE 18 SEP 2000		2. REPORT TYPE		3. DATES COVERED 00-00-2000 to 00-00-2000	
4. TITLE AND SUBTITLE Research Aircraft Observations and Numerical Simulations of a Warm Front Approaching Vancouver Island				5a. CONTRACT NUMBER	
				5b. GRANT NUMBER	
				5c. PROGRAM ELEMENT NUMBER	
6. AUTHOR(S)				5d. PROJECT NUMBER	
				5e. TASK NUMBER	
				5f. WORK UNIT NUMBER	
7. PERFORMING ORGANIZATION NAME(S) AND ADDRESS(ES) Naval Research Laboratory, 7 Grace Hopper Ave., Stop 2, Monterey, CA, 93943-5502				8. PERFORMING ORGANIZATION REPORT NUMBER	
9. SPONSORING/MONITORING AGENCY NAME(S) AND ADDRESS(ES)				10. SPONSOR/MONITOR'S ACRONYM(S)	
				11. SPONSOR/MONITOR'S REPORT NUMBER(S)	
12. DISTRIBUTION/AVAILABILITY STATEMENT Approved for public release; distribution unlimited					
13. SUPPLEMENTARY NOTES					
14. ABSTRACT see report					
15. SUBJECT TERMS					
16. SECURITY CLASSIFICATION OF:			17. LIMITATION OF ABSTRACT Same as Report (SAR)	18. NUMBER OF PAGES 21	19a. NAME OF RESPONSIBLE PERSON
a. REPORT unclassified	b. ABSTRACT unclassified	c. THIS PAGE unclassified			

falling frontal systems impinging on complex three-dimensional orography in the presence of time-dependent flow are still not well understood. Furthermore, one of the goals of the recent COAST experiment has been to utilize both intensive observations and high-resolution numerical model simulations to study the impact of the steep coastal terrain of the Pacific Northwest on fronts and cyclones.

Important aspects of airflow response to a topographic obstacle can be characterized in terms of a Froude number, $Fr = U/Nh_m$, where U is the incident wind speed, N is the Brunt–Väisälä frequency, and h_m is the barrier or relevant scale height. Low-level flow tends to be blocked by a topographic barrier when $Fr < 1$ (e.g., Smith 1979), which leads to flow splitting and downstream vortex shedding (Smolarkiewicz and Rotunno 1989; Schär and Durran 1997) and upstream deceleration (Pierrehumbert and Wyman 1985). In the presence of rotation, the e -folding of the mountain-normal component deceleration region is on order of the Rossby deformation radius ($L_R = Nh_m/f$). A balanced mesoscale response to the blocked flow results in the formation of an upstream barrier jet of width $O(L_R)$ (e.g., Pierrehumbert and Wyman 1985; Overland and Bond 1993). Overland and Bond (1995) document the flow along Vancouver Island for a case in which cold air that exited from the Strait of Juan de Fuca was blocked south of the topography and resulted in a strong barrier jet formation. For $Fr > 1$, airflow can readily ascend and descend the obstacle, and generation of gravity waves ensues in the linear regime (e.g., Smith 1989). Scale analyses based on parameters such as Fr have been fairly successful for rather idealized conditions (e.g., Overland and Bond 1995). However, simple scale analysis is likely to be inapplicable for many aspects of landfalling storms. In general, these situations include factors neglected in conventional scale analysis, notably time-dependent and diabatic effects. In the present case, the response of the incident flow to coastal terrain, particularly Vancouver Island, was also complicated by a pre-existing mass of cool air along the coast. This air mass was constrained by the coastal terrain but had originated in the interior of the Pacific Northwest, and hence its characteristics were not solely controlled by orographic effects. The interactions between the above-mentioned factors make it very difficult to diagnose conceptually the mechanisms responsible for the evolution of storm features in the coastal zone.

Observational and numerical studies have shown that fronts tend to weaken on the windward sides of mountains and strengthen on the lee slopes (Blumen and Gross 1987; Williams et al. 1992; Gross 1994). These studies attribute the frontolysis upstream along the windward slope and frontogenesis along the lee slope to the divergence pattern resulting from the upstream blocking of the ageostrophic cross-mountain circulation. The greatest response of a front to a mesoscale obstacle occurs when Fr is small, the front is shallow as in the

case of typical warm fronts, the cross-frontal gradient is large, the front-normal velocity is small, and a large mean state stratification exists (Schumann 1987). Braun et al. (1999) found that the balanced barrier-oriented jet may be superimposed on the frontal jet to produce large wind speeds in the coastal zone.

There have been numerous investigations of the influence of mesoscale topography on cold (e.g., Davies 1984; Volkert et al. 1991; Overland and Bond 1993) and occluded fronts (e.g., Grønås 1995; Steenburgh and Mass 1996) using numerical and observational approaches. However, the influence of topography on warm frontal dynamics has received considerably less attention. Heymsfield (1979) used Doppler radar observations to document the circulations associated with precipitation bands accompanying a warm front over the central United States. Some studies (e.g., Wakimoto et al. 1992; Neiman et al. 1993) have examined the warm front as one of the dynamically important structures associated with deep or especially rapidly developing oceanic cyclones. A warm front off the Washington coast (in the region of the present study) has been analyzed previously by Locatelli and Hobbs (1987) and Hertzman et al. (1988). The former paper documented the mesoscale structure; the latter showed how the vertical wind shear organized the distribution of precipitation. While Parsons and Hobbs (1983) surveyed rainfall and radar reflectivity patterns as two warm fronts interacted with the coastal terrain of Washington State, there has not been a detailed study of the modification of a landfalling warm front as it approached coastal terrain in the manner of Braun et al. (1997) for a cold front. The latter study documented changes in the prefrontal low-level flow that appeared to be due to the upstream influence of the coastal terrain, with consequences for the structure of a narrow cold-frontal rainband. Doyle and Shapiro (2000) recently documented the topographic deformation of a landfalling warm front over Norway that played a key role in the development of a severe windstorm in the lee of complex orography.

The objective of the present study is to document the case of 9–10 December 1995 from COAST featuring a warm front as it made landfall in the Pacific Northwest. Our focus is on the nearshore low-level flow on the southwest side of Vancouver Island and the changes in the approaching front. This case merits in-depth study because it represents a common, yet challenging, forecast situation (in anticipating changes in frontal structure and propagation), and because of the availability of a unique set of mean, turbulence, and Doppler radar data collected by the P-3 aircraft complemented by high-resolution numerical simulations. The specific objectives of this study are to (i) document the structure and dynamics of the warm front as it made landfall in a region of steep coastal orography; (ii) examine orographic blocking of the warm front in presence of complex coastal mesoscale forcing, which includes a nearly continuous low-level cold-air source from the Strait of

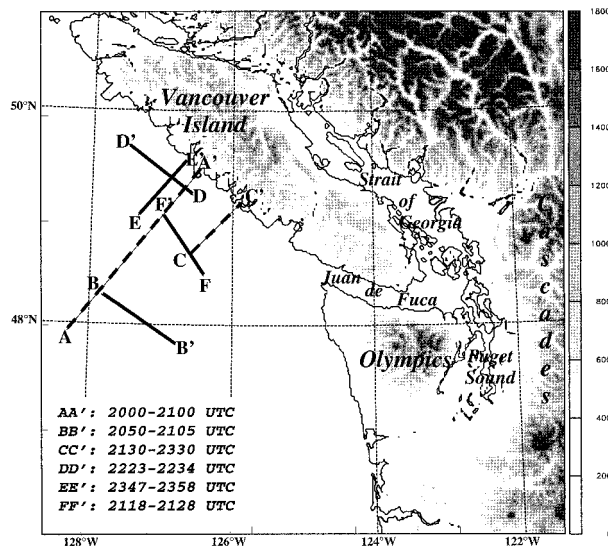


FIG. 1. Geographic region for NOAA P-3 research aircraft measurements including Vancouver Island and vicinity. Selected flight legs are shown with solid lines and locations of vertical cross sections with dashed lines. The corresponding times for the legs are shown for 9 Dec 1995. The terrain height (m) is indicated by the shading.

Juan de Fuca; (iii) characterize the nature of the turbulence in the coastal environment associated with the landfalling warm front; and (iv) evaluate the capability of a nonhydrostatic numerical model to simulate mesoscale aspects of a landfalling warm front. The synoptic-scale setting is discussed in section 2. The numerical model is described in section 3. Section 4 contains the analysis of the research aircraft observations. The simulation results are presented in section 5. Section 6 contains the conclusions of the study.

2. Synoptic setting

The purpose of this section is to provide a context for the mesoscale analysis that follows, rather than to provide a detailed description of the evolution of the synoptic-scale flow. A map of the area of interest is shown in Fig. 1. The most important topographical features are the two-dimensional barrier (typical crest height ~ 1200 m) represented by Vancouver Island, the bell-shaped Olympic Mountains, and in between, the sea level gap of the Strait of Juan de Fuca. Figure 1 also includes the locations of flight legs and cross sections referred to later in the paper. We focus on conditions at 0000 UTC 10 December, since the most relevant aircraft observations to our analysis were collected between approximately 2000 UTC on 9 December and 0100 UTC on 10 December. Synoptic analysis should be considered complementary to the synoptic background previously provided by Colle and Mass (2000). They also analyzed P-3 observations and high-resolution simulation for 9–10 December 1995, but with the intent of documenting and understanding gap flow

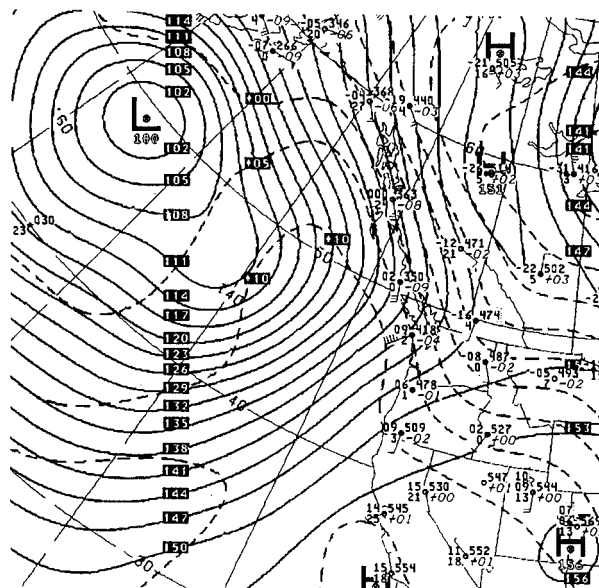


FIG. 2. The 850-mb analysis for 0000 UTC 10 Dec 1995 from NCEP (from Colle and Mass 2000).

out of the Strait of Juan de Fuca, rather than the present study's focus on the warm front and nearshore flow along Vancouver Island.

The synoptic-scale conditions for 0000 UTC 10 December are summarized using the 850-mb analysis from the National Centers for Environmental Prediction (NCEP) (Fig. 2) and an infrared image from the Geostationary Operational Environmental Satellite (GOES-W) satellite (Fig. 3). Figure 2 shows a low-level baroclinic zone with a total temperature difference of $\sim 25^{\circ}\text{C}$ and a wind shift of $\sim 50^{\circ}$ moving onshore into Washington State and British Columbia. Warm air associated with southwesterly flow followed a period of approximately 6 days with a modified arctic air mass at

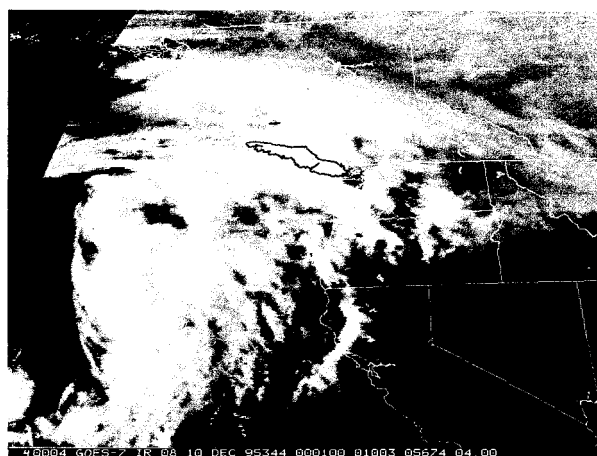


FIG. 3. Infrared satellite image from GOES-W valid at 0001 UTC 10 Dec 1995.

low levels over the Pacific Northwest. The satellite image (Fig. 3) shows largely overcast conditions in the warm sector south and southwest of Vancouver Island. A northwest–southeast-oriented band of higher cloud tops (and presumably enhanced precipitation) was located in the nearshore region on the southwest side of Vancouver Island.

A series of surface analyses are now presented to illustrate the progression of the warm front toward Vancouver Island. The warm front here depicts the southern edge of the low-level wind shift zone and baroclinic zone. The analysis for 1800 UTC 9 December (Fig. 4a) shows the warm front extended in a roughly east–south–east to west–northwest orientation from the northern coast of Oregon toward the low center located off the left (west) edge of the map. At this time, it is estimated to have been about 300 km offshore of Vancouver Island. By 0000 UTC 10 December (Fig. 4b), the front had made only slight progress in the immediate vicinity of the west coast, but its offshore portion had moved well north to a position about 90 km offshore of the central portion of Vancouver Island. The front's propagation in this region slowed markedly in the next 6 h. As shown by the map for 0600 UTC 10 December (Fig. 4c), the front now extended from just south of the northwest tip of Washington State to near the northwest tip of Vancouver Island, remaining typically ~ 30 km offshore of the bulk of Vancouver Island. Based on these estimated positions, the movement of the front toward the central portion of Vancouver Island slowed from an average of $\sim 10 \text{ m s}^{-1}$ in the 6 h preceding 0000 UTC, to an average of $\sim 3 \text{ m s}^{-1}$ in the 6 h after 0000 UTC. During this period, the warm front was oriented more or less parallel to Vancouver Island.

The situation presented here represents a common scenario during the cool season in the Pacific Northwest. Southerly geostrophic flow and warm advection on the synoptic scale tends to result in noticeably strong and persistent alongshore winds, and relatively cool temperatures, along the coast of Vancouver Island, as compared with the ambient offshore conditions.

3. Numerical model description

The atmospheric portion of the navy's Coupled Ocean–Atmospheric Mesoscale Prediction System (COAMPS) (Hodur 1997) is applied in this study. The model makes use of finite-difference approximations to

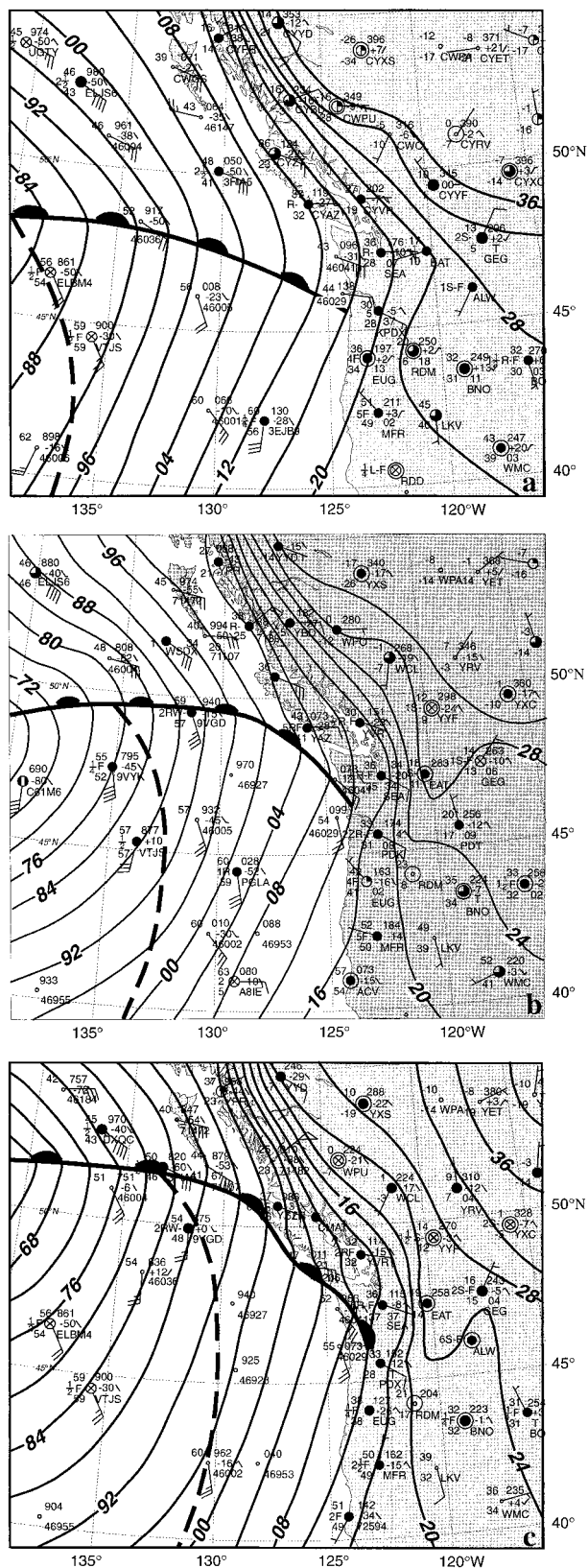


FIG. 4. Surface analyses for (a) 1800 UTC 9 Dec, (b) 0000 UTC 10 Dec, and (c) 0600 UTC 10 Dec 1995. The isobar interval is 4 hPa. Ship and buoy reports are plotted using the standard convention. The temperature and dew point temperature are shown in Fahrenheit, and the pressure is plotted in hPa using conventional notation. One full barb corresponds to 5 m s^{-1} . Visibility is plotted in statute miles. The dashed line indicates a trough in the sea level pressure. Numerous land stations are omitted for clarity.

represent the fully compressible, nonhydrostatic equations that govern atmospheric motions. In this application, the equations are solved in three dimensions on four nested grid meshes with a terrain-following vertical coordinate, σ (Gal-Chen and Somerville 1975). The finite difference schemes are of second-order accuracy in time and space. Efficient integration of the compressible equations is accomplished through the use of a time-splitting technique that features a semi-implicit treatment in the vertical for the acoustic modes (Klemp and Wilhelmson 1978; Durran and Klemp 1983).

The parameterization of short- and longwave radiation processes is accomplished following Harshvardhan et al. (1987). The planetary boundary layer and free-atmospheric turbulent mixing and diffusion are modeled using a prognostic equation for the turbulent kinetic energy (TKE), e , budget based on the level-2.5 formulation of Mellor and Yamada (1982) as follows:

$$\frac{\partial e}{\partial t} = -u \frac{\partial e}{\partial x} - v \frac{\partial e}{\partial y} - \sigma \frac{\partial e}{\partial \sigma} + \text{BP} + \text{SP} + D + K_H \nabla^4 e - \varepsilon, \quad (1)$$

where u and v are the horizontal wind velocity components, BP is the buoyancy production, SP is the shear production, D is the subgrid-scale vertical mixing, K_H is the horizontal diffusion coefficient, and ε is the dissipation rate. The buoyancy production is defined as

$$\text{BP} = -\frac{GgK_h}{\theta} \frac{\partial \theta_v}{\partial \sigma}, \quad (2)$$

where G is the coordinate transformation metric defined as $\partial \sigma / \partial z$, g is the acceleration of gravity, K_h is the vertical eddy mixing coefficient for heat, and θ is the potential temperature. The shear production is defined as

$$\text{SP} = K_m \left[\left(G \frac{\partial u}{\partial \sigma} \right)^2 + \left(G \frac{\partial v}{\partial \sigma} \right)^2 \right], \quad (3)$$

where K_m is the vertical eddy mixing coefficient for momentum. The dissipation rate is parameterized in (1) as

$$\varepsilon = \frac{\alpha}{\ell} e^{3/2}, \quad (4)$$

where α is a constant of 0.17, and ℓ is the mixing length following Mellor and Yamada (1982). Accurate representation of the TKE is necessary because the eddy diffusivity coefficients for heat and momentum, K_h and K_m , are directly proportional to $e^{1/2}$. Countergradient correction terms to the vertical fluxes are included for the potential temperature and water vapor equations following Therry and LaCarrère (1983). The surface fluxes are computed following the Louis (1979) formulation, which makes use of Monin–Obukhov similarity theory. A force-restore method is used to parameterize the surface energy budget. The subgrid-scale moist convective processes are parameterized using an approach follow-

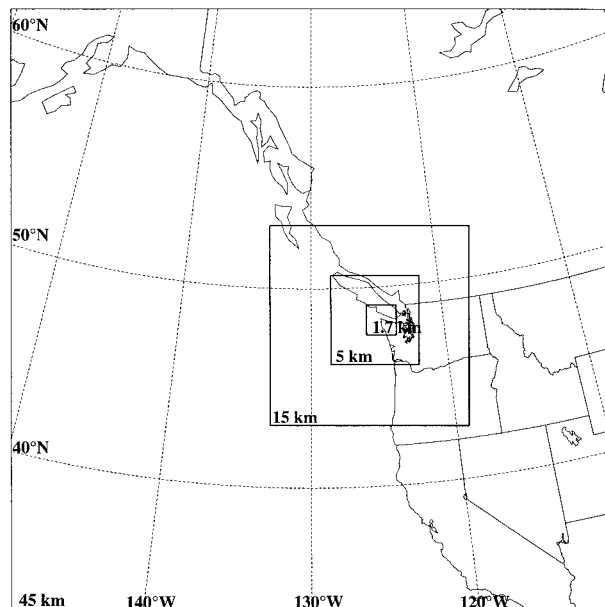


FIG. 5. Numerical model computational domain for grid meshes 1 ($\Delta x = 45$ km), 2 ($\Delta x = 15$ km), 3 ($\Delta x = 5$ km), and 4 ($\Delta x = 1.67$ km).

ing Kain and Fritsch (1990). The grid-scale evolution of the moist processes are explicitly predicted from budget equations for cloud water, cloud ice, raindrops, snow flakes, and water vapor (Rutledge and Hobbs 1983).

The domain configuration used to simulate the land-falling front event includes four horizontally nested grids of 73×73 , 73×73 , 97×97 , and 97×97 points, respectively. The locations of the grid meshes are shown in Fig. 5. The horizontal grid increment of the computational meshes are 45, 15, 5, and 1.7 km, respectively. The model top is at 31 km with 40 irregularly spaced vertical levels and 19 levels in the lowest 1.5 km to adequately resolve the boundary layer processes. Reflection of waves at the upper boundary is mitigated by a gravity wave absorbing layer using a Rayleigh damping technique in the upper portion of the model domain.

An incremental update data assimilation procedure, which retains mesoscale circulations in the analysis increment fields, is used to initialize a 30-h COAMPS simulation beginning at 0000 UTC 9 December 1995. The initial state for the nonhydrostatic model is created from multivariate optimum interpolation analyses of upper-air sounding, surface, aircraft, and satellite data that are quality controlled and blended with the 12-h COAMPS forecast fields based on the incremental update analysis methodology. Lateral boundary conditions are constructed using Navy Operational Global Analysis and Prediction System (Hogan and Rosmond 1991) forecast fields following Davies (1976). The use of COAMPS in this type of application closely emulates a real-time numerical prediction system in spite of the

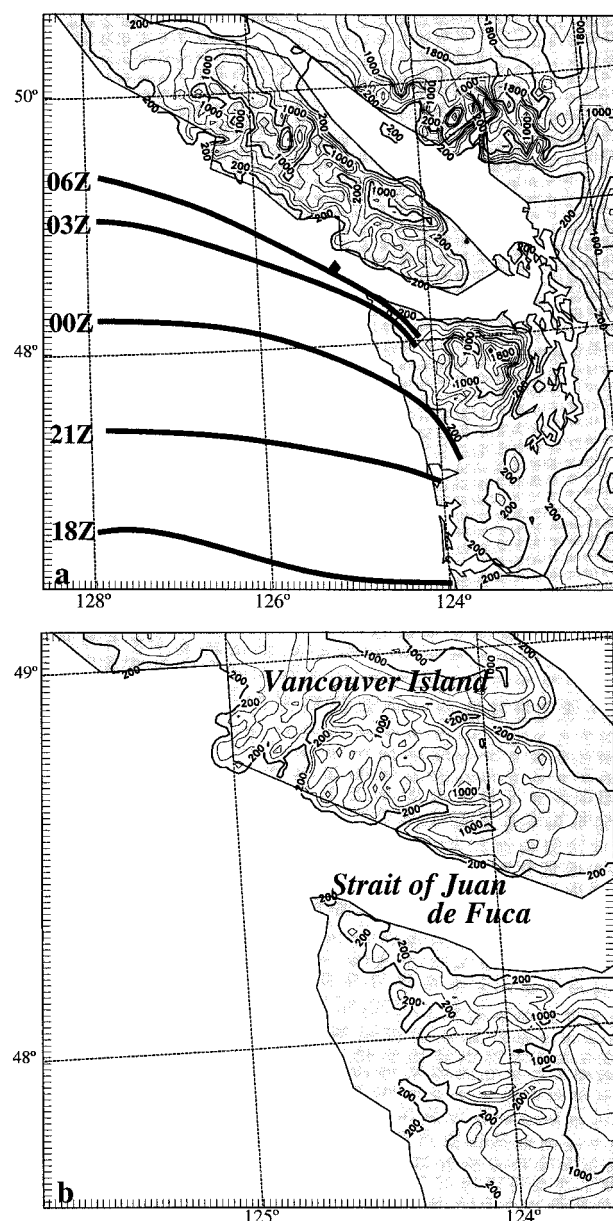


FIG. 6. Model topography for the (a) third ($\Delta x = 5$ km) and (b) fourth grid meshes ($\Delta x = 1.67$ km). The contour interval is 200 m. The simulated surface warm front isochrones are displayed in (a). The times (UTC) for the frontal positions on 9–10 Dec 1995 are noted in (a).

simulations being performed in a hindcast mode. The topographic data are based on the U.S. Defense Mapping Agency's 100-m resolution dataset. The model terrain fields for the third ($\Delta x = 5$ km) and fourth meshes ($\Delta x = 1.7$ km), shown in Figs. 6a and 6b, respectively, indicate that notable topographic features such as the Olympic Range and the complex topography of Vancouver Island are well represented.

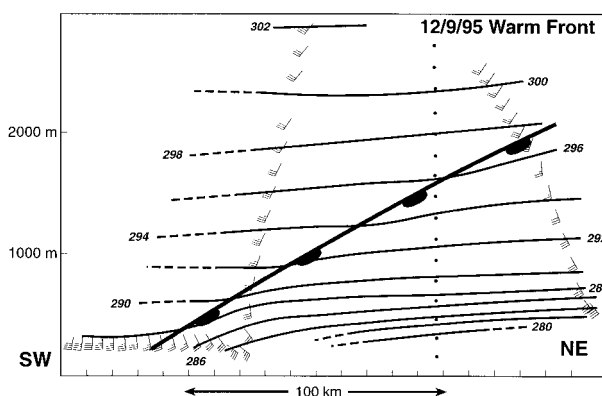


FIG. 7. Vertical cross section of potential temperature (isotherm interval 2 K) and wind barbs (each full barb represents 5 m s^{-1}) based on selected flight-level data collected between ~ 2000 and 2100 UTC 9 Dec and projected onto an axis along 40° – 220° normal to and moving with the front (AA' in Fig. 1). Isentropes are dashed in data-sparse areas. The dots show the location of the thermodynamic data from a dropsonde.

4. Research aircraft observations

a. Mesoscale structure

The objective of this section is to document two aspects of this event, the warm front as it neared land and the nearshore flow along Vancouver Island. This analysis relies on flight-level and Doppler radar data collected by the P-3. Although the primary goal of the flight was to collect radar data, and hence the flight-level data coverage was spotty, the latter measurements are important because they provide thermodynamic information. The Doppler radar data from selected legs was edited and synthesized following the techniques outlined by Yu and Smull (2000). The result was three-dimensional fields of horizontal and vertical winds, and radar reflectivity, on a grid with a spacing of 0.25 km in the vertical and 1.5 km in the horizontal. Because of the smoothing inherent to the synthesis, the resolvable scales of motion are approximately 0.75 and 4 km in the vertical and horizontal, respectively.

We begin by presenting the structure of the warm front at 2000–2100 UTC, while it was still ~ 200 km offshore of Vancouver Island. The flight-level data (Fig. 7) shows a zone of enhanced baroclinity at the leading edge of the front (defined as the upper boundary of the wind shear zone) near the surface. Below about a kilometer, this baroclinic zone included a change in potential temperature (θ) of ~ 4 K and a windshift of $\sim 40^\circ$ over a horizontal scale of 20–30 km. The gradual nature of this transition near the surface (which was well resolved by flight-level measurements during penetration of the front at ~ 300 m) contrasts with the 1–5-km scale common to cold fronts (Browning and Harrold 1970, among many others). The slope of the warm front below 2 km was roughly 1:100, to the extent it can be determined given the limited amount of data.

Another depiction of the warm front at this time is

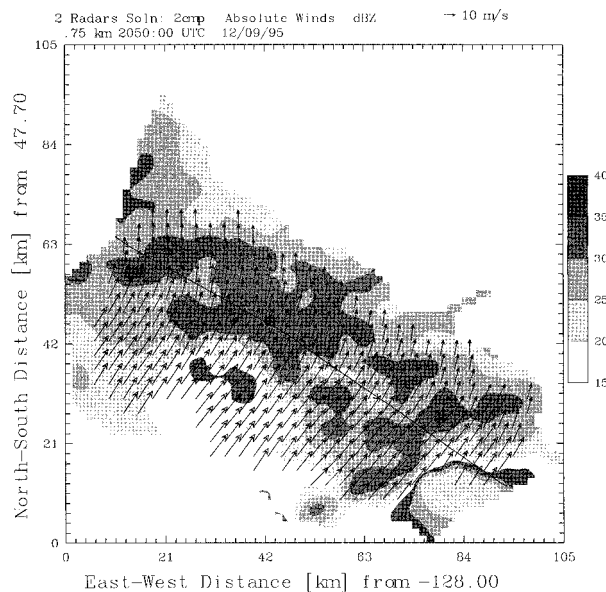


FIG. 8. Radar reflectivity (dBZ; grayscale indicated to the right of the figure) and ground-relative winds at the 750-m level from the 2050–2105 UTC leg (BB' in Fig. 1).

provided by the Doppler radar observations from a northwest–southeast-oriented leg between 2050 and 2105 UTC. A horizontal section at the 750-m level (Fig. 8) shows the gradual wind shift associated with the front was accompanied by a 30-km-wide band of enhanced precipitation, with radar reflectivities of 25–30 dBZ. A vertical cross section normal to the front (Fig. 9) shows that the echo top was ~ 4 km and the suggestion of a “bright band” at 3 km, which was near the freezing level. The flow in the plane of the section indicates a modest updraft of $\sim 1 \text{ m s}^{-1}$; however, this is near the quantitative limits of the analysis capabilities. The primary vertical wind shear in this section is in the component normal to the section (and along the front). The shear involves the transition between the low-level southeasterlies of $\sim 8 \text{ m s}^{-1}$ at the lowest resolved level of 500 m within and ahead of the frontal zone, and the advancing and overlying southwesterlies. The location of the warm front shown in Fig. 9 was determined by the vertical shear of the alongfrontal wind component.

We now turn our attention toward the structure of the low-level flow along Vancouver Island prior to the land-fall of the front. The flight-level data collected during maneuvers between about 2130 and 2330 UTC while maneuvering for radar and upper-level legs in the near-shore region have been collapsed onto a vertical cross section oriented normal to Vancouver Island (Fig. 10). These observations show cool, alongshore flow below about 700 m with potentially warmer onshore-directed flow above. Substantial vertical wind shear and static stability separated these flows in a distinct transition zone only about 100 m thick. However, very little baroclinity was present as the transition zone was virtually

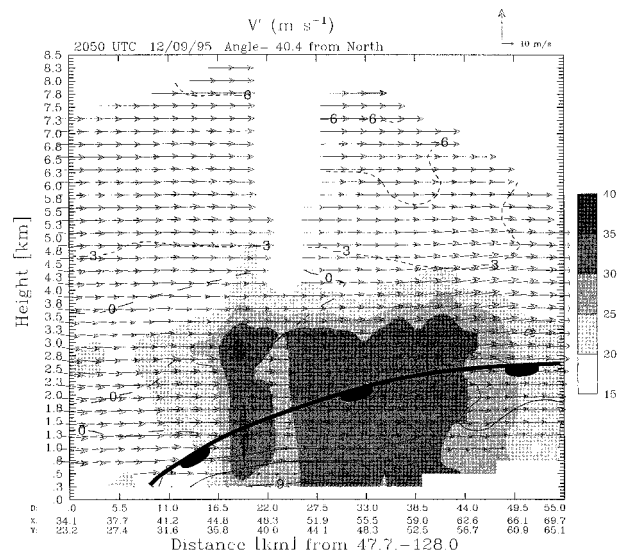


FIG. 9. Vertical cross section of radar reflectivity (shading; dBZ), ground-relative flow in the plane of the section (arrows), and ground-relative flow normal to the section (solid lines, m s^{-1}) oriented along 40° – 220° from the 2050–2105 UTC leg (BB' in Fig. 1).

flat from near the shore to at least 60 km offshore. The level nature of the transition zone contrasts with the sloping baroclinic zone associated with the classical barrier jet and cold-air damming (e.g., Bell and Bosart 1988).

The Doppler radar observations collected about 30 km offshore of Vancouver Island between 2233 and 2244 UTC are consistent with this cross section based on flight-level data. Horizontal sections at 500 and 1000 m (Figs. 11a and 11b, respectively) show that the wind direction varied relatively little in the horizontal, with the exception of the northeastern portion of the domain

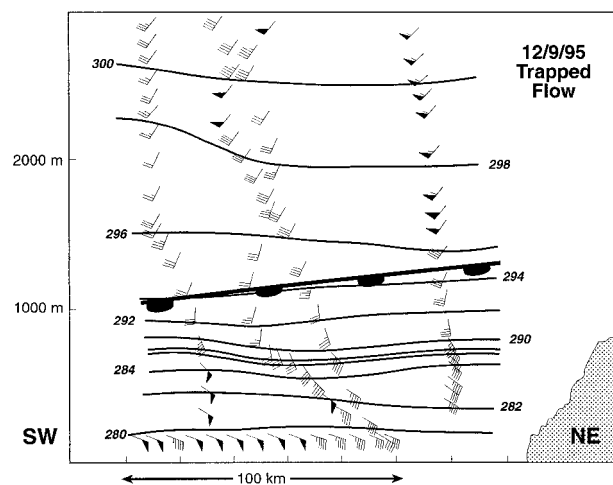


FIG. 10. As in Fig. 7, but for flight-level observations collected between 2130 and 2330 UTC and projected onto a time-space adjusted axis along 45° – 225° approximately normal to Vancouver Island (CC' in Fig. 1). Land is represented by the stippled region.

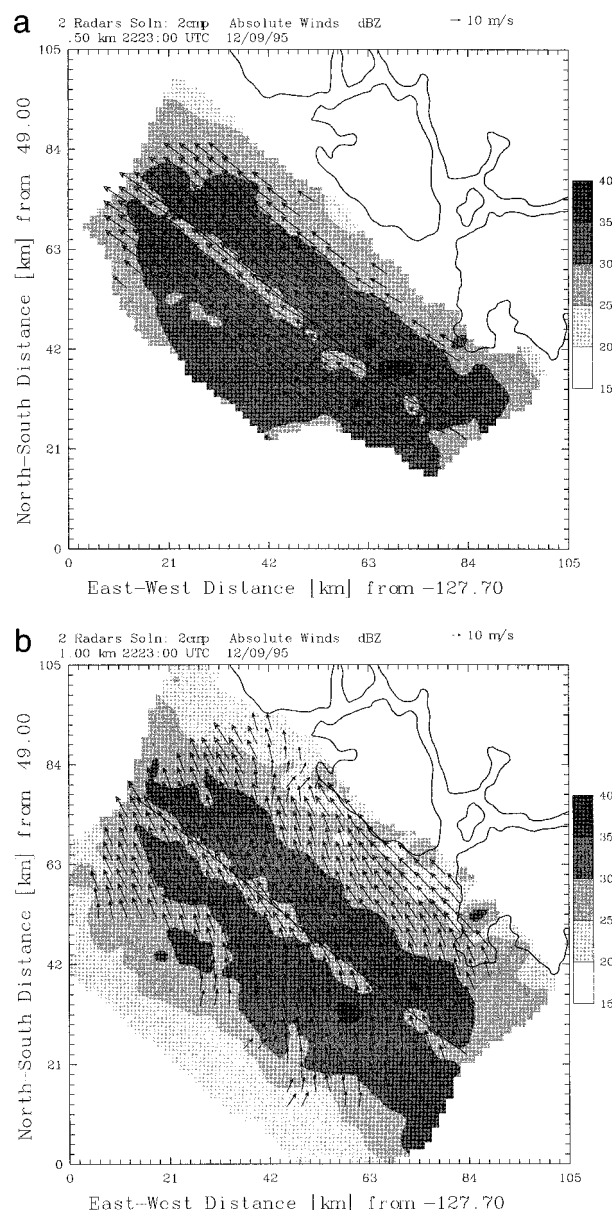


FIG. 11. As in Fig. 8, but for the 2223–2234 UTC leg (DD' in Fig. 1) at (a) 500 and (b) 1000 m.

at 1000 m, where the flow was oriented along the axis of nearby Vancouver Island. These and other horizontal sections suggest that the flow was organized into quasi-horizontal flat sheets with the greatest vertical shear near the 750-m level. Figures 11a and 11b also show a 40-km-wide band of higher radar reflectivity centered near the flight track that was 30 km offshore. This band has no obvious connection to any low-level feature and may reflect the influence of the elevated portion of the warm front moving over the cool, nearshore air mass. A representative vertical cross section (Fig. 12) oriented normal to Vancouver Island suggests that slightly enhanced upward motion was occurring above 1 km near the flight

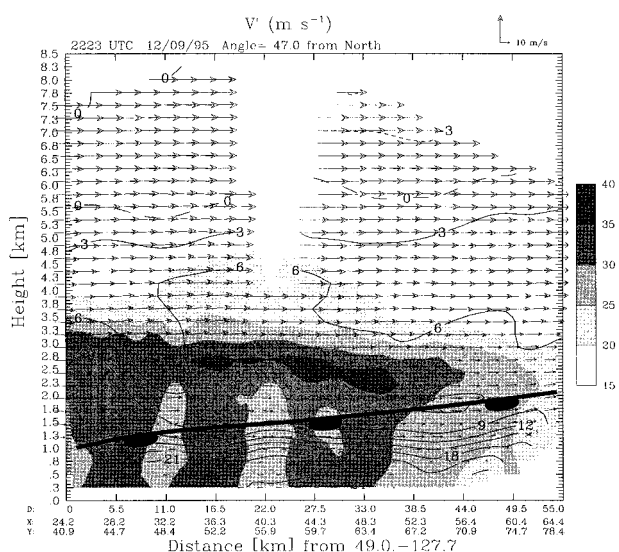


FIG. 12. As in Fig. 9, but for the 2223–2234 UTC leg (DD' in Fig. 1).

track. However, this result is somewhat tentative because the signal is weak and approaching the inherent limits of the analysis. The lighter precipitation in the immediate vicinity of Vancouver Island may also be a result of locally lower humidities near the surface due to a downslope component to the flow, as indicated by the surface winds shown in Figs. 4a–c.

We conclude this section with presentation of results from Doppler radar measurements collected on a north-east–southwest-oriented leg between 2347 and 2358 UTC. This leg was the latest portion of the flight that included a survey of the front, which at this time was located near the southwest end of the leg roughly 90 km offshore of Vancouver Island. A horizontal section at 750 m (Fig. 13) shows a similar transition in the winds as found 3 h previously (Fig. 8), when the front was farther offshore. The later observations do indicate that the wind shift was somewhat more concentrated, into a zone roughly 10 km wide. The front at this later time marked the seaward extent of continuous moderate precipitation, instead of the localized precipitation maximum found earlier. A vertical cross section from the later leg (Fig. 14) suggests that the slope of the lowest kilometer or so of the front had steepened considerably. There was also substantially more vertical wind shear in the alongfront component as compared with the previous leg (Fig. 9), due to the superposition of the shear associated with the front and trapped flow. The bright band, apparent in the reflectivity fields in Figs. 12 and 14, was located in the 2.4–2.8-km layer and was associated with the freezing level encountered by the research aircraft between 2.6 and 2.8 km.

b. Turbulence characteristics

The gust probe-radome system aboard the P-3 provided flight-level measurements at a rate of 40 Hz during

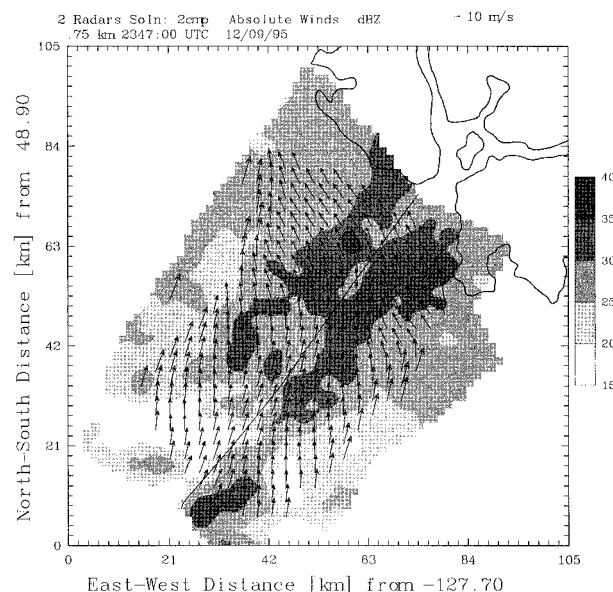


FIG. 13. As in Fig. 8, but for the 2347–2358 UTC leg (EE' in Fig. 1).

the flight. The high-frequency measurements from selected legs were processed following the techniques outlined by Khelif et al. (1999). The results offered a rare opportunity to document the turbulence that occurred in various sectors of the front and the nearshore flow. Our focus here is on the turbulent-scale fluctuations in the wind, namely, the momentum fluxes and TKE. Our objectives are to examine the relationships between the mean and turbulent aspects of the low-level flow, and to assess the ability of COAMPS in simulating the turbulent character of the flow.

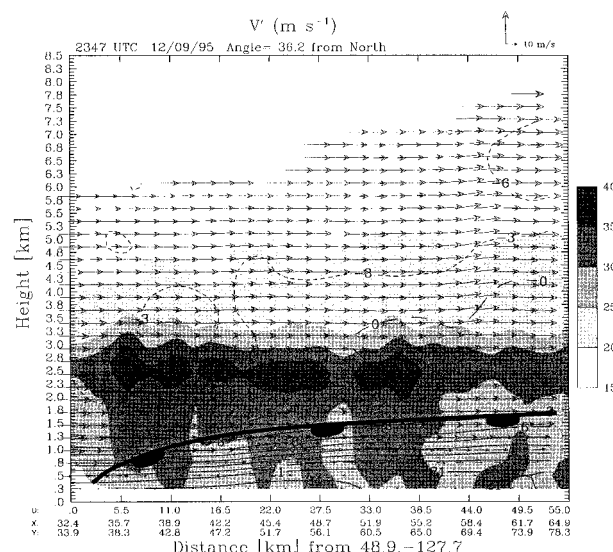


FIG. 14. As in Fig. 9, but for the 2347–2358 UTC leg (EE' in Fig. 1).

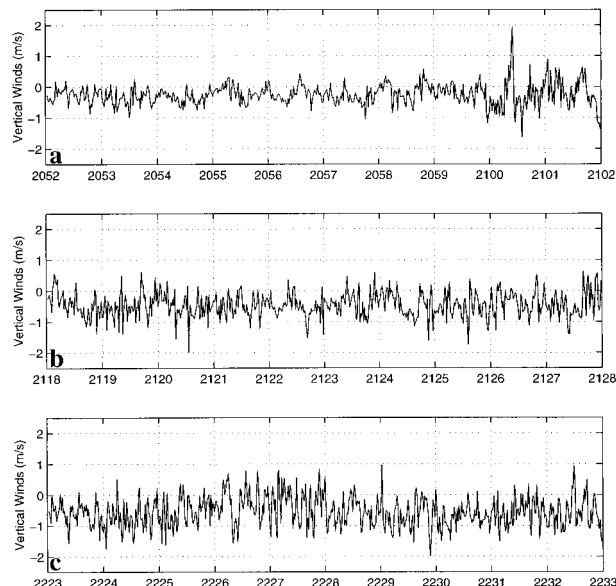


FIG. 15. Time series of 1-Hz values of vertical velocity at flight level from (a) 2052–2102 UTC (AA' in Fig. 1) in the warm sector, (b) 2118–2128 UTC (FF' in Fig. 1) in the frontal zone, and (c) 2223–2233 UTC (EE' in Fig. 1) in the trapped flow.

Differences in the magnitude and nature of the turbulence in the warm sector, frontal zone, and nearshore flow are illustrated via time series of vertical velocity (w) during level legs of about 10-min duration. These time series show that fluctuations in w were typically $\sim 0.2 \text{ m s}^{-1}$ in the warm sector (Fig. 15a) with a single prominent updraft of $\sim 2 \text{ m s}^{-1}$, in the frontal zone $\sim 0.5 \text{ m s}^{-1}$ (Fig. 15b) with about a half-dozen notable downdrafts, and $\sim 0.7 \text{ m s}^{-1}$ in the nearshore region with no obvious skewness to the prominent extrema (Fig. 15c). Mean statistics for these legs, and a repeat leg in the nearshore region, are summarized in Table 1. As suggested by the w time series of Fig. 15, the overall intensity of the turbulence, as gauged by the magnitude of the TKE, was least in the warm sector and greatest in the nearshore region. The relatively weak intensity of the turbulence in the warm sector is no surprise; this sector had the warmest air, weakest wind speeds, and least vertical wind shear and therefore the least amount of surface buoyancy and shear production of turbulence of any of the three regions. The frontal zone and near-

TABLE 1. Mean turbulence statistics. Wind speeds are m s^{-1} ; $u'w'$, $v'w'$, and TKE are in $\text{m}^2 \text{ s}^{-2}$. The quantities $u'w'$ and $v'w'$ represent the magnitude of the cross-wind and along-wind momentum fluxes, respectively.

Leg/altitude	Mean speed/ dir.	$u'w'$	$v'w'$	TKE
Warm sector (335 m)	12.8/172°	0.04	0.11	1.0
Frontal zone (350 m)	21.7/119°	0.12	0.15	1.7
Near shore (155 m)	19.0/120°	−0.48	−0.01	2.2
Near shore (177 m)	20.9/122°	−0.44	0.01	2.2

shore regions had similar wind speeds and θ , and it is not obvious why the nearshore region had significantly greater TKE. It is possible that much of the production of TKE was due to surface layer buoyancy and shear production, and the weaker TKE observed in the frontal zone than the nearshore region was merely a consequence of the former being at a higher altitude and thus farther removed from this source. Another possible explanation is that the turbulence in the frontal zone was suppressed by the greater static stability locally relative to the nearshore region. The close correspondence between the results for the two nearshore legs indicates that at least the mean statistics for these legs are reliable.

Table 1 also shows systematic differences between the momentum fluxes in the three regions. In particular, the ratio of the along-wind to cross-wind momentum fluxes was small ($\ll 1$) in the warm sector, intermediate (~ 1) in the frontal zone, and large ($\gg 1$) in the nearshore region. The dissimilarities in these ratios are largely due to differences in the correlation coefficients between the along-wind (u') and cross-wind (v') fluctuations with w' , rather than the magnitudes of the variance in u and v . The mean wind profiles presented in the previous section indicate that the component with the greater momentum flux is associated with the component that had the greatest mean vertical shear, as previously observed (e.g., Brost et al. 1982).

Further insight on the character of the turbulence in this situation can be gained from consideration of its spectral properties. Here we focus on the differences between the frontal zone and nearshore regions in the cospectra and quadrature in the fluctuations between the v and w . The cospectra for the frontal zone (Fig. 16a) indicate that the main contribution to the net momentum flux was occurring at frequencies corresponding to wavelengths between roughly 150 and 600 m. Mostly longer wavelengths were involved in the bulk of the quadrature between v' and w' in the frontal zone (Fig. 16b). The systematic sense to the quadrature at wavelengths greater than roughly 300 m suggests the presence of gravity waves. As shown in the previous section, the frontal zone included significant vertical wind shear, which for this leg was largely in the cross-wind component at flight level. This shear is likely to have been a source of energy for these waves. Following Metcalf (1975), the ratios of the quadrature and cospectra between the u' and w' , to their counterparts with v' , indicate that the gravity waves and momentum fluxes were oriented at angles of 58° and 53° , respectively, with respect to the mean wind. The breaking of the gravity waves may account for the shorter spatial scales found in the momentum fluxes, that is, the cospectra (Fig. 16a). As indicated by Table 1, the mean cross-wind momentum flux was near zero in the nearshore region, and Fig. 17a shows this was because of compensation between negative $v'w'$ at scales greater than ~ 1 km and mostly positive $v'w'$ at shorter scales. Considerable cancellation was also occurring in the quadrature between v'

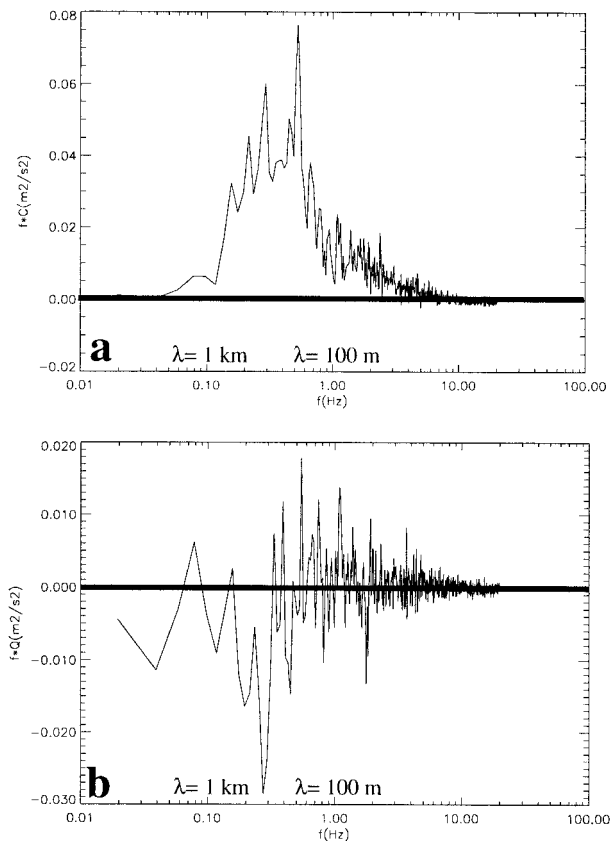


FIG. 16. Cospectrum of the cross-wind (v') and vertical (w') wind components in the frontal zone (FF' in Fig. 1) as a function of wavelength (on a log scale) shown in (a). The quadrature between v' and w' is shown in (b).

and w' in the nearshore region (Fig. 17b), and for that matter between u' and w' (not shown), suggesting relatively incoherent wave activity. These results for the nearshore region are grossly consistent with the mean wind field presented earlier, which indicate little vertical shear at low levels.

5. Numerical model results

a. Control simulation

A 30-h simulation of the landfalling warm front using COAMPS was initialized based on the 0000 UTC 9 December 1995 data. The 700-hPa geopotential heights and winds valid at 0000 UTC 10 December (24-h simulation time) for the third grid mesh ($\Delta x = 5$ km) are shown in Fig. 18. Strong southwesterly flow and warm-air advection prevailed during this time period over the Pacific Northwest ahead of a large-amplitude trough and developing baroclinic wave. The model-simulated geopotential height, temperature, and wind fields are in reasonable agreement with the radiosonde observations. For example, the model simulation accurately distinguishes between the strong ~ 20 m s^{-1} southwesterly

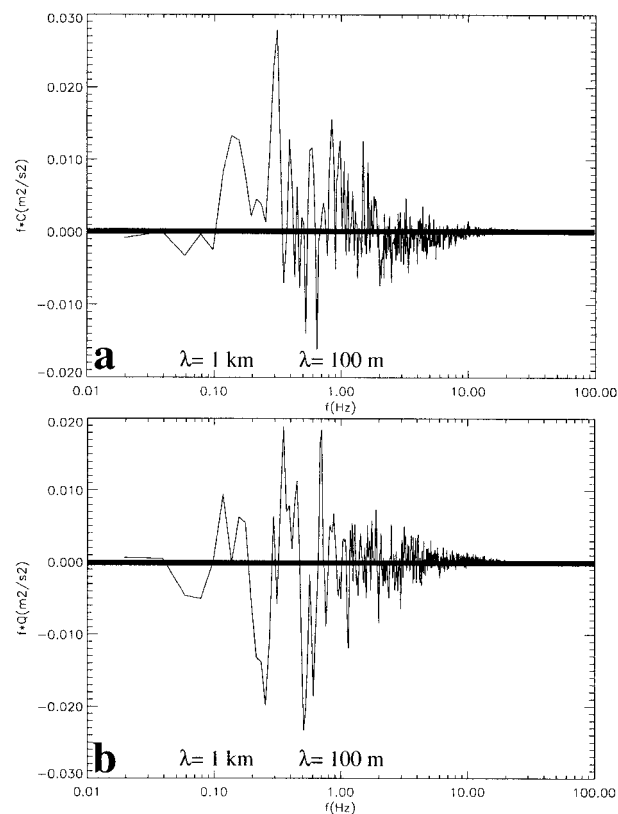


FIG. 17. As in Fig. 1b, except for the trapped flow (EE' in Fig. 1).

flow at Quillayute, Washington, and the weaker $\sim 8 \text{ m s}^{-1}$ westerlies at 700 hPa in southern British Columbia.

The model simulated 10-m wind and 500-m potential temperature fields for 2100 UTC 9 December (21 h) and 0300 UTC 10 December (27 h) are displayed in Fig. 19. At 2100 UTC 9 December (21 h), the near-surface southeasterly flow (Fig. 19a) is positioned to the north of the surface warm front (Fig. 19a), which is associated with a frontal baroclinic zone of $\sim 6 \text{ K}$ at 500 m (Fig. 19b). Shallow cold easterly flow is present within the Strait of Juan de Fuca and extends westward along the southern edge of Vancouver Island, resulting in a secondary baroclinic zone at the western edge of the strait (Fig. 19b). The northward movement of the simulated near-surface warm front is slowed considerably such that by 0300 UTC 10 December (27 h) the surface front location ranges from $\sim 25 \text{ km}$ offshore of Vancouver Island, near the exit of the Strait of Juan de Fuca, to $\sim 500 \text{ km}$ offshore, farther westward (Figs. 19c,d). The blocking of the warm front as it approaches Vancouver Island is highlighted by the isochrones of the surface front (Fig. 6a), based on the 10-m thermal and vorticity fields. In this case, research aircraft data cannot provide general validation for the near-surface wind field. However, the surface wind reports from available ships of opportunity and buoys provide limited validation for the model-simulated low-level wind field

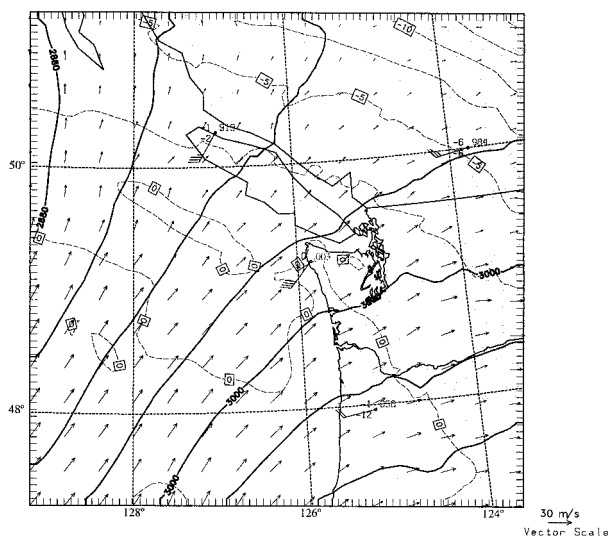


FIG. 18. Simulated 700-hPa geopotential height (solid), temperature (dashed), and wind vector fields valid at 0000 UTC 10 Dec 1995 (24 h). The contour intervals are 30 m and 2.5°C . Wind, temperature, dewpoint, and geopotential height radiosonde observations are plotted using the conventional notation with a full barb representing 5 m s^{-1} .

characterized by (i) the horizontal wind shear associated with surface warm front, (ii) the relatively strong ($\sim 15 \text{ m s}^{-1}$) east-southeasterly flow north of the surface warm front that is trapped between the front and the steep topography of Vancouver Island, and (iii) the weaker southerly flow in the warm sector.

The evolution of the maximum of the magnitude of the potential temperature gradient at 100 m along the front and the near-surface warm front propagation speed are summarized in Table 2 for the 1800 UTC 9 December–0400 UTC 10 December time period. The low-level ($\sim 100 \text{ m}$) potential temperature gradient associated with the warm frontal zone increased in time as the warm front approached Vancouver Island to a maximum of $\sim 14.2 \text{ K } 100 \text{ km}^{-1}$ at 0200 UTC 10 December 1995. A localized secondary maximum in the frontal gradient occurs when the warm front is located along the southern edge of the gap exit of the Strait of Juan de Fuca, which results in a superposition of the frontal and cold gap flow thermal gradients (Fig. 19b). After 0200 UTC, portions of the low-level thermal gradient associated with the front weaken slowly as the gap flow becomes shallow and the warm front advances to the north (Fig. 19d). The central and western segment of the front strengthens prior to landfall as apparent in the 0300 UTC 10 December 1995 thermal field. In general, the propagation speed of the front progressively slows after 2100 UTC 9 December as the warm front approaches the topography of Vancouver Island. The propagation speed just prior to landfall at 0400 UTC is reduced to approximately one-third of the speed well upstream of the topography (2100 UTC).

The vertical structure of the warm front, which in-

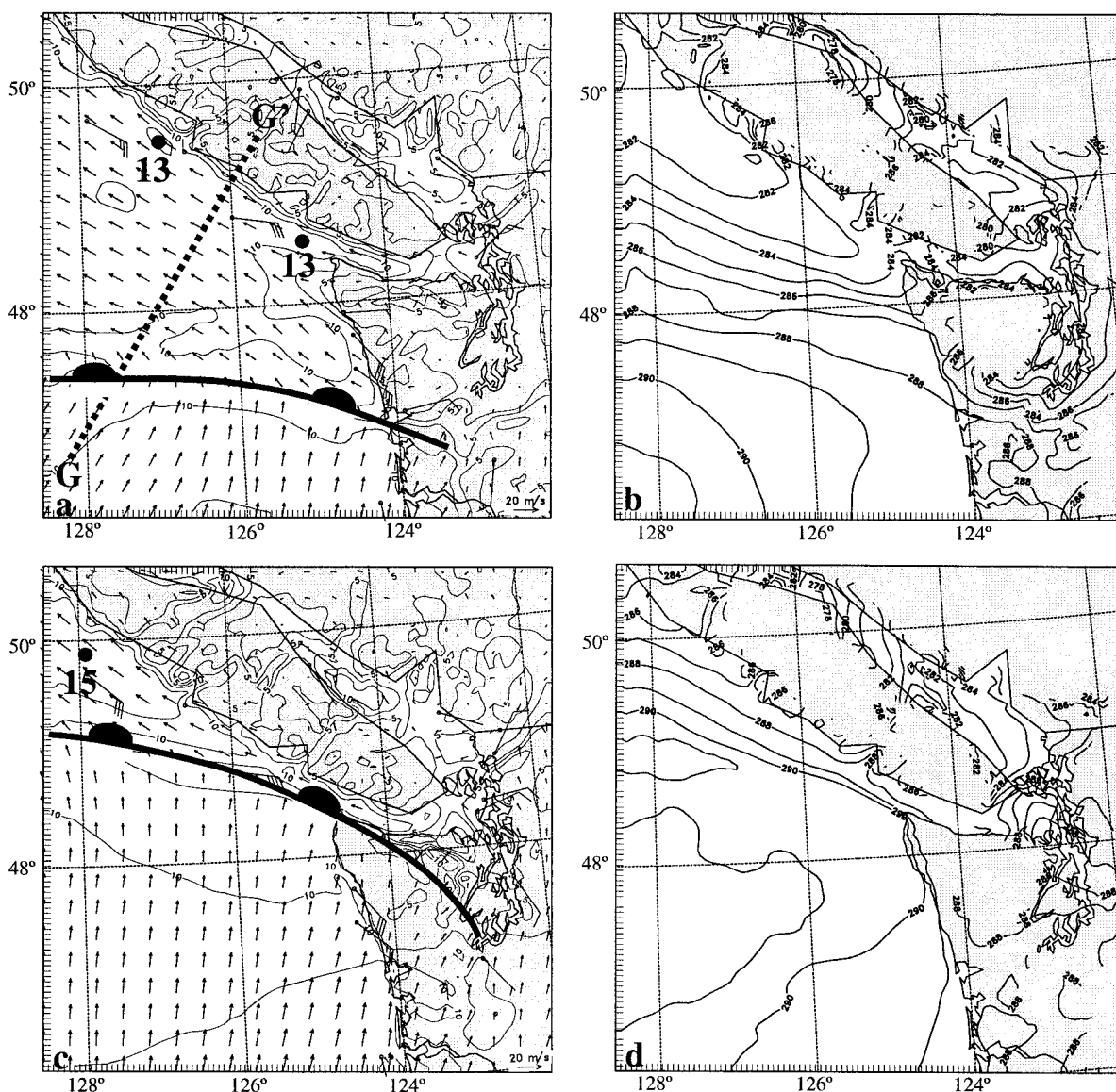


FIG. 19. The model-simulated (a) 10-m winds and (b) 500-m potential temperature fields for 2100 UTC 9 Dec (21 h) and (c) 10-m winds and (d) 500-m potential temperature fields for 0300 UTC 10 Dec 1995 (27 h). The isotach interval in (a) and (c) is 2.5 m s^{-1} . The isotherm interval in (b) and (d) is 1 K . Selected surface wind observations are displayed in (a) and (c) with one full barb representing 5 m s^{-1} .

cludes the easterly flow that comprises the trapped flow region, is illustrated in Fig. 20 by the vertical cross sections for 2100 UTC 9 December (21 h) constructed along line GG' (cross section location shown in Fig. 19a). The warm front location, as determined by the vertical shear of the alongfrontal wind component, is shown in Fig. 20b. The vertical section of potential temperature (Fig. 20a) indicates that the depth of the trapped flow north of the warm front is $\sim 500 \text{ m}$, which is $\sim 200 \text{ m}$ lower than indicated by research aircraft observations at this time, but of a similar character (see Figs. 7 and 10). An isentropic cross section along line CC' (cross section location shown in Fig. 1) for 2200 UTC 9 De-

cember (22 h), shown in Fig. 21, reveals many similarities with the analysis based on the in situ aircraft observations (Fig. 10). In particular, both the aircraft observations and the simulation show that the transition zone between the trapped and overlying flow is relatively thin and flat. However, the model-simulated barrier jet (Fig. 20b) is $\sim 5\text{--}7 \text{ m s}^{-1}$ weaker than measured by the research aircraft, in spite of a reasonably accurate simulated synoptic-scale evolution. The simulation depicts a sloped baroclinic zone and enhanced low-level static stability associated with the warm front. The sloped cyclonic shear zone associated with the warm front is apparent in the section displaying the wind com-

TABLE 2. Hourly simulated maximum of the magnitude of potential temperature gradient and warm frontal propagation speed at 100 m.

Time	$ \nabla\theta _{\max}$ (K (100 km) $^{-1}$)	Propagation speed (m s $^{-1}$)
1800 UTC 9 Dec	9.2	9.7
1900 UTC	11.4	8.3
2000 UTC	11.3	9.2
2100 UTC	10.2	10.3
2200 UTC	10.8	9.2
2300 UTC	10.3	8.3
0000 UTC 10 Dec	11.8	7.5
0100 UTC	12.3	6.9
0200 UTC	14.2	5.5
0300 UTC	12.5	4.5
0400 UTC	8.6	3.2

ponent parallel to Vancouver Island and normal to the cross section plane (Fig. 20b).

The trapped flow is characterized by the $\sim 14 \text{ m s}^{-1}$ low-level jet that extends from the surface to $\sim 500 \text{ m}$ and is oriented parallel to the front. The simulated trapped flow is considerably weaker than the observed flow of $20\text{--}25 \text{ m s}^{-1}$. Significant vertical shear in the front-normal wind component (Fig. 20c) extends through the sloping warm front inversion. It is noteworthy that the flow immediately upstream of the Vancouver Island topography is weak or even offshore in contrast to cold-air damming situations, which frequently are characterized by an appreciable mountain-normal component that enhances low-level cooling and damming (e.g., Bell and Bosart 1988; Doyle and Warner 1990). The far-field upstream flow is characterized by $N \sim 0.017 \text{ s}^{-1}$ and $U \sim 14 \text{ m s}^{-1}$, which for an 800-m-high barrier yields $Fr \sim 1.0$. An Fr of approximately unity was computed from the research aircraft data for this case. Overland and Bond (1995) hypothesize that when $R_0/Fr > 1$, where $R_0 = U/fL$ and L is the mountain half width, the largest blocking response with maximum enhancement of the along-barrier flow may occur when $Fr \sim 1$, similar to the conditions for the present case.

The model-simulated TKE field constructed along line GG' (Fig. 19a), shown in Fig. 22, indicates low-level maxima in the nearshore trapped flow and frontal zones. Budget analysis (not shown) suggests that the primary TKE maximum, located near the shore of Vancouver Island, is predominantly driven by shear in the mountain parallel wind component (e.g., see Fig. 20b). Additionally, buoyancy effects contribute to TKE generation in this region because of the upward surface heat

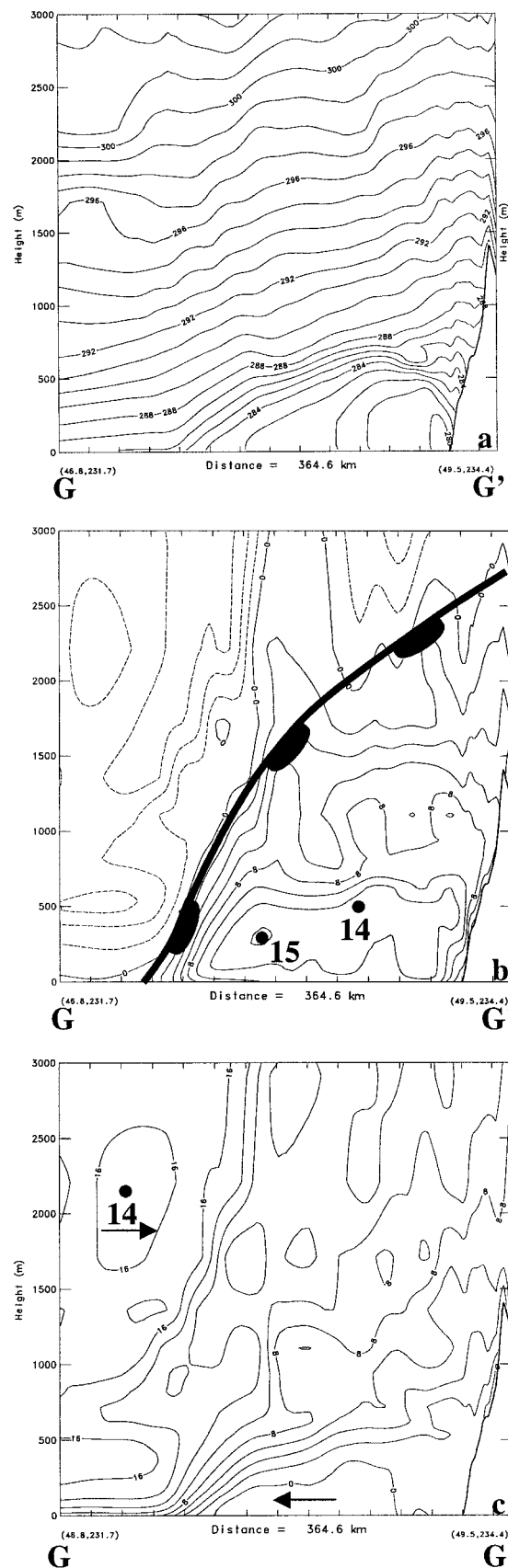


FIG. 20. Vertical cross section of (a) potential temperature, (b) coast-parallel (section normal) wind component, and (c) coast-normal (section parallel) wind component along line GG' (Fig. 19a) valid at 2100 UTC 9 Dec 1995 (21 h). The isotherm interval is 1 K in (a) and the isotach interval is 2 m s $^{-1}$ in (b) and (c). Wind maxima are denoted by the maximum speed labels in (b) and (c).

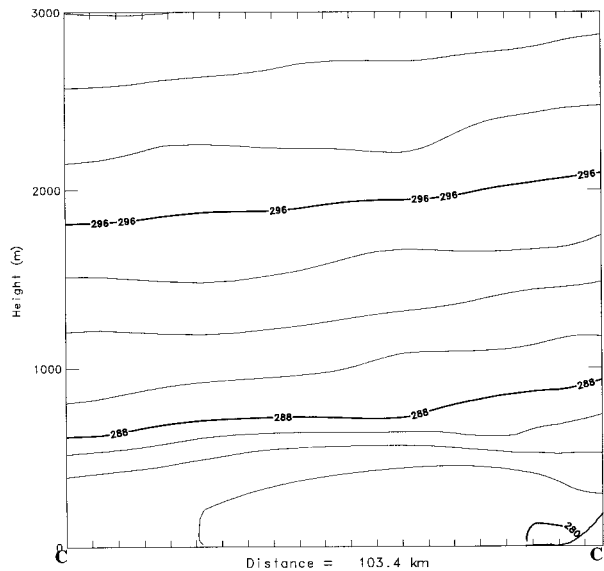


FIG. 21. Vertical cross section of potential temperature along line CC' (Fig. 1) valid at 2200 UTC 9 Dec 1995 (22 h). The isotherm interval is 2 K.

fluxes associated with the cold boundary layer ($\sim 6^{\circ}$ – 7°C) (Fig. 20b), which originates in the Strait of Juan de Fuca gap flow, that lies above the warmer sea surface ($\sim 8^{\circ}$ – 9°C). The secondary TKE maximum, which is positioned within the sloping warm frontal zone, is due mainly to the large shear in the low-level winds (Figs. 20b,c). The buoyancy term acts as a sink of TKE in the frontal zone due to the stable conditions. The maximum of $\sim 1.4 \text{ m}^2 \text{ s}^{-2}$ at 200 m above ground level (AGL) along the coast of Vancouver Island is comparable to the $2.2 \text{ m}^2 \text{ s}^{-2}$ derived from the research aircraft data (e.g., see Table 1). The secondary maximum of $0.8 \text{ m}^2 \text{ s}^{-2}$ in the simulated frontal zone is once again in relative agreement with the secondary maximum computed from the flight-level data of $1.7 \text{ m}^2 \text{ s}^{-2}$. However, the simulated TKE in the warm sector at 300 m AGL is $\sim 0.2 \text{ m}^2 \text{ s}^{-2}$, which notably is less than the $1.0 \text{ m}^2 \text{ s}^{-2}$ calculated for the ambient warm sector conditions based on the research aircraft data. There is a considerable scale discrepancy between the model simulation, which made use of a 5-km grid increment on the third mesh, and the research aircraft TKE observations, which used 50–100-km legs for the computation of the fluxes. Additionally, the simulated barrier jet is slightly weaker than observed, which likely results in an underestimate of the shear and buoyancy production in the trapped flow. However, the model captures the overall correct turbulent character of the flow that includes the largest TKE values in the nearshore region and the least in the warm sector.

The model-simulated instantaneous precipitation and wind fields for 500 m above mean sea level (MSL) valid at 0000–0200 UTC 10 December (24 h) are shown in Fig. 23. The model-simulated radar reflectivity, which

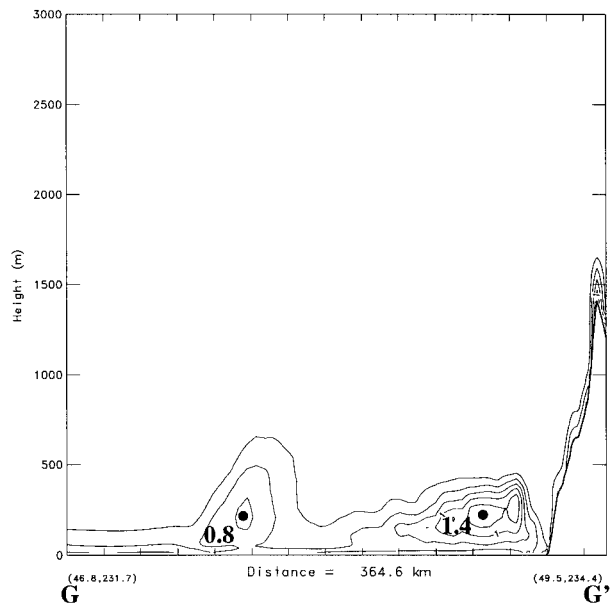
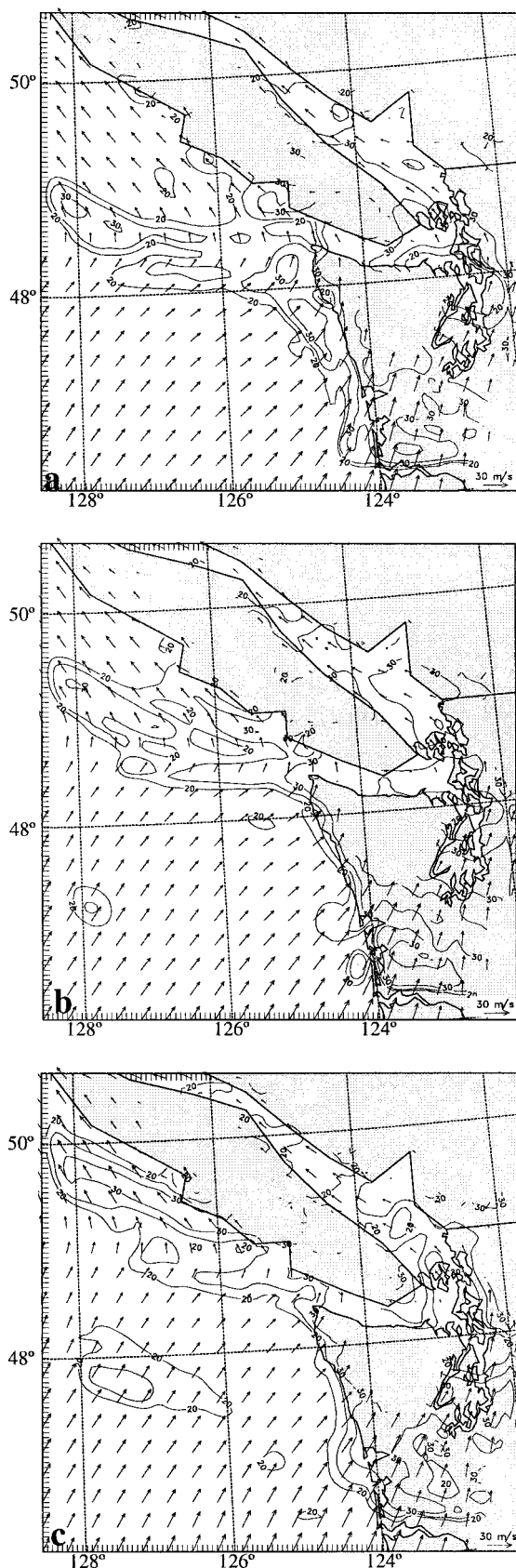


FIG. 22. Vertical cross section of TKE along line GG' (Fig. 19a) valid at 2100 UTC 9 Dec 1995 (21 h) for the third grid mesh ($\Delta x = 5 \text{ km}$). The contour interval is $0.25 \text{ m}^2 \text{ s}^{-2}$.

is computed based on the explicitly predicted bulk microphysical parameters, cloud water, rainwater, ice crystals, and snowflakes, indicates a band of precipitation associated with the warm front embedded in the horizontal deformation zone at 0000 UTC (Fig. 23a). Two enhanced regions of precipitation rate are apparent offshore of Vancouver Island and are in good agreement with the research aircraft reflectivity derived from the Doppler radar for 2230 UTC (e.g., see Fig. 11a). The model simulated reflectivity maxima are $\sim 30 \text{ dBZ}$, and also in reasonable agreement with the observations. However, the position of the simulated warm frontal precipitation band is ~ 20 – 30 km farther offshore than indicated by the research aircraft observations. Additionally, the simulated precipitation band is located on the warm side of the cyclonic vorticity maximum, in contrast to the observed precipitation, which tended to be greater on the cool side of the front. As the front moves toward Vancouver Island, the $>30\text{-dBZ}$ region becomes more continuous, indicative of a slight intensification of the precipitation band (Figs. 23b,c).

The Strait of Juan de Fuca flow dynamics is investigated using the simulation results from grid mesh 4 ($\Delta x = 1.67 \text{ km}$) valid at 1700 UTC 9 December (17 h), shown in Fig. 24. The characteristics and structure of the gap flow have been previously investigated by Colle and Mass (2000) using research aircraft data and Mesoscale Model 5 (MM5) numerical model simulations. They found significant three-dimensional effects including cross-gap flow and abrupt acceleration of the easterly flow near the exit of the strait. In this situation, the gap outflow bears some resemblance to shallow fluid expansion fan dynamics, as evinced by the numerical



simulations. However, Colle and Mass note that the acceleration near the gap exit is apparently linked with mountain wave dynamics associated with downslope flow in the lee of the surrounding terrain. Further examination of the gap outflow in this case enables a comparison between the observations, and the two model simulations using COAMPS and MM5. The COAMPS simulated winds at 100 m MSL valid at 1700 UTC 9 December (17 h), shown in Fig. 24a, indicate acceleration at the strait exit leading to a wind speed maximum of $\sim 16 \text{ m s}^{-1}$ located $\sim 75 \text{ km}$ downstream of the gap exit region. The position of the wind speed maximum is in good agreement with the research flight level data shown in Fig. 25. The depth of the simulated cold easterlies is $\sim 200 \text{ m}$ shallower than observed and considerably different from the Colle and Mass simulation, which was deeper than observed. The location of the wind speed maximum near the middle of the strait exit, well away from upstream topography, and cross section analysis of the flow indicate that the acceleration is not likely linked to descent in the lee of the local topography.

The vertical cross sections of potential temperature and along-cross section wind speed, shown in Figs. 24b,c (constructed along line HH' shown in Fig. 24a), suggest the acceleration and wind speed maximum near the strait exit are consistent with expansion fan dynamics. Vertical descent of the isentropes over a depth of 300 m is apparent to the west of the strait exit (Fig. 24b) in a region where the flow, initially constrained in the strait, diverges horizontally. Calculations of a single-layer Fr, defined as

$$Fr = \frac{U}{(g'h)^{0.5}}, \quad (5)$$

where U is the velocity, g' is reduced gravity, and h is the layer depth, supports the expansion fan and transcritical behavior of the flow. For example, upstream of the strait exit, the along-gap velocity is $\sim 8 \text{ m s}^{-1}$, $h \sim 400 \text{ m}$, and $g' \sim 0.3$, which results in a $Fr \sim 0.7$. Farther downstream of the exit, $U \sim 15 \text{ m s}^{-1}$, $h \sim 200 \text{ m}$, and $g' \sim 0.1$, indicating a flow transition to supercritical with a $Fr \sim 3.4$. Despite the time-variant forcing and three-dimensional effects associated with this complex flow, the transcritical expansion fan dynamics is consistent with the formation of the wind maxima near the strait exit.

b. Sensitivity experiments

The numerical simulation discussed above suggests that the low-level portion of the warm front slowed

←

FIG. 23. Model-simulated radar reflectivity and winds at 500 m based on the explicitly predicted microphysical variables valid at 0000 UTC 10 Dec 1995 (24 h). The contour interval is 5 dBZ. Wind vectors are plotted every five model grid points.

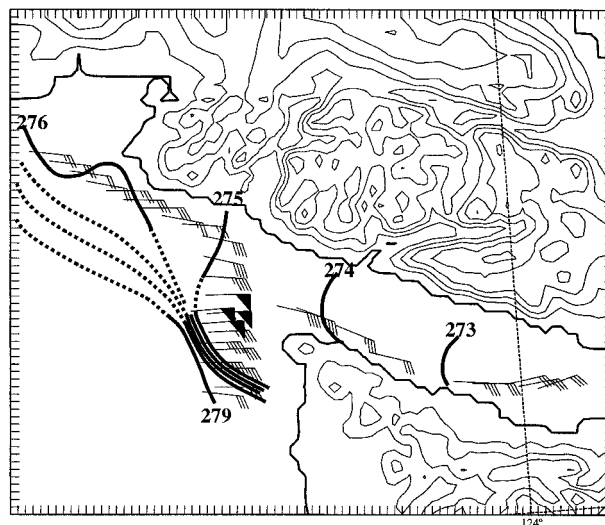
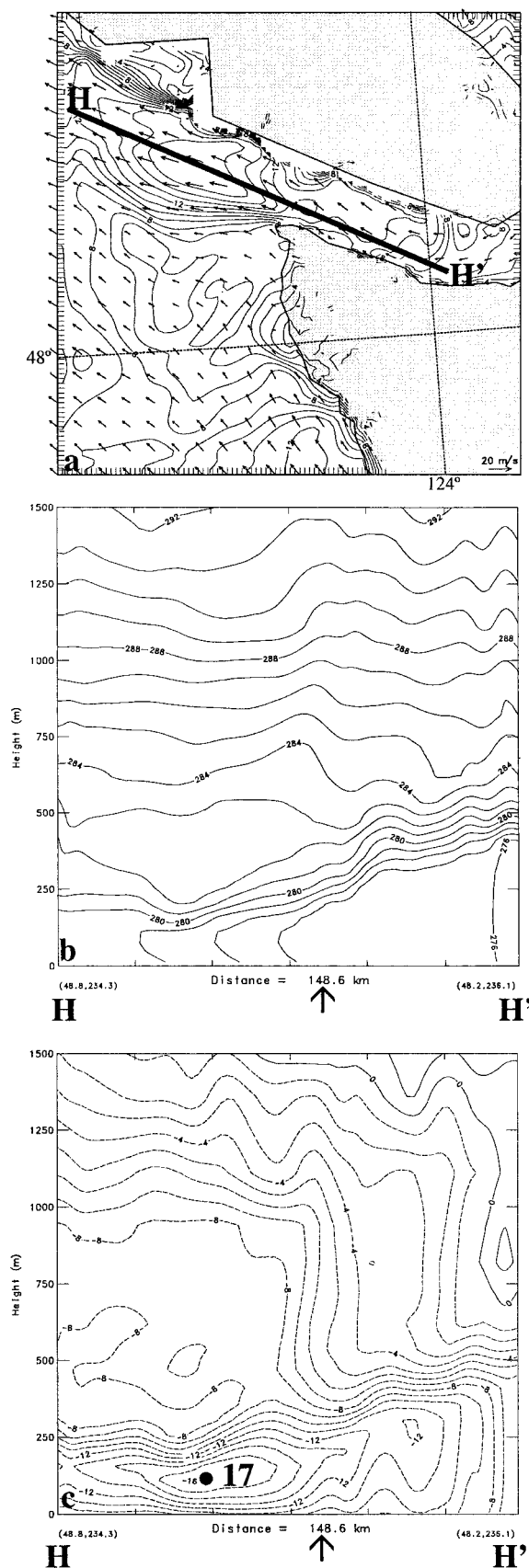


FIG. 25. Wind and potential temperature observations at 300 m based on the NOAA WP-3D flight-level data for 1600–1800 UTC 9 Dec 1995. Isentropes (K) are dashed in data-sparse areas. The isentropes are plotted every 1 K.

considerably upon approaching Vancouver Island in agreement with the observations presented above. The role of (i) orographic blocking by the steep Vancouver Island topography and (ii) the cold and dense air mass residing in the nearshore area of Vancouver Island as mechanisms for frontal impedance were investigated using two sensitivity experiments. The first experiment eliminates the topography of Vancouver Island, as indicated by the model terrain field in Fig. 26a. The topography for the second sensitivity experiment, shown in Fig. 27a, contains an orographic barrier ~ 800 m high in the western portion of the Strait of Juan de Fuca in order to impede the low-level easterly flow. The modifications to the orography were introduced at the initialization time, 0000 UTC 9 December 1995.

The 10-m wind field for the simulation without any Vancouver Island topography (Fig. 26b) indicates that the position of the near-surface warm front is located near that of the control simulation at 0300 UTC 10 December 1995 (Fig. 19c). However, the surface front isochrones (Fig. 26a) indicate a more rapid northward movement of the front relative to the control simulation (Fig. 6a) after 0300 UTC. By 0600 UTC 10 December 1995, the warm front in the simulation without any Vancouver Island topography is located ~ 50 km to the north of control simulation front. The low-level easterly flow

FIG. 24. (a) Model-simulated 100-m (MSL) winds valid at 1700 UTC 9 Dec 1995 (17 h) for nested grid mesh 4. Vertical cross section along line HH' (projection plane location shown in (a)) of (b) potential temperature and (c) along strait (section parallel) wind component. The isotach interval in (a) and (c) is 1 m s^{-1} . The isotherm interval is 1 K in (b). The arrow in (b) and (c) indicates the location of the strait exit.

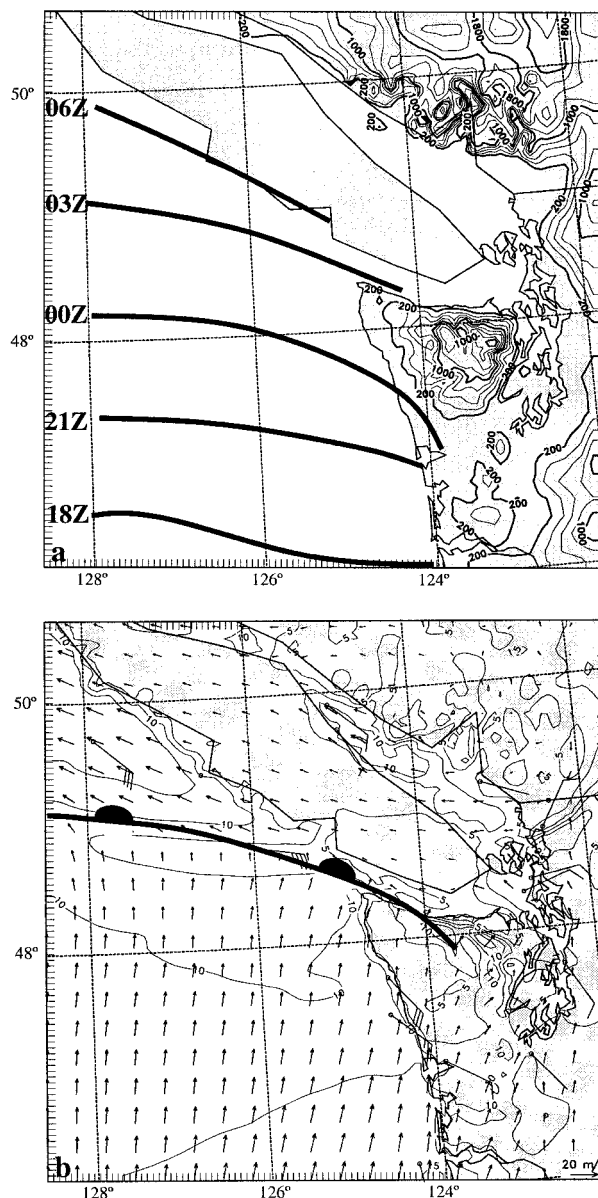


FIG. 26. (a) Terrain and surface warm front isochrones for the sensitivity experiment with the Vancouver Island topography removed. (b) Model simulated 10-m winds with an isotach interval of 2.5 m s^{-1} valid at 0300 UTC 10 Dec 1995 (27 h). Selected surface wind observations are displayed in (b) with one full barb representing 5 m s^{-1} . The times for the frontal position on 9–10 Dec 1995 are (UTC) is noted in (a).

is strengthened over Vancouver Island, creating a shallow cold air mass positioned to the north of the warm front, in the simulation with the topography removed. This experiment indicates the blocking of the warm front by the orography of Vancouver Island is greater than the blocking associated with the additional low-level cold air in the absence of the orography. Given the mean state conditions that were present upstream of the orography, strong blocking would not be anticipated.

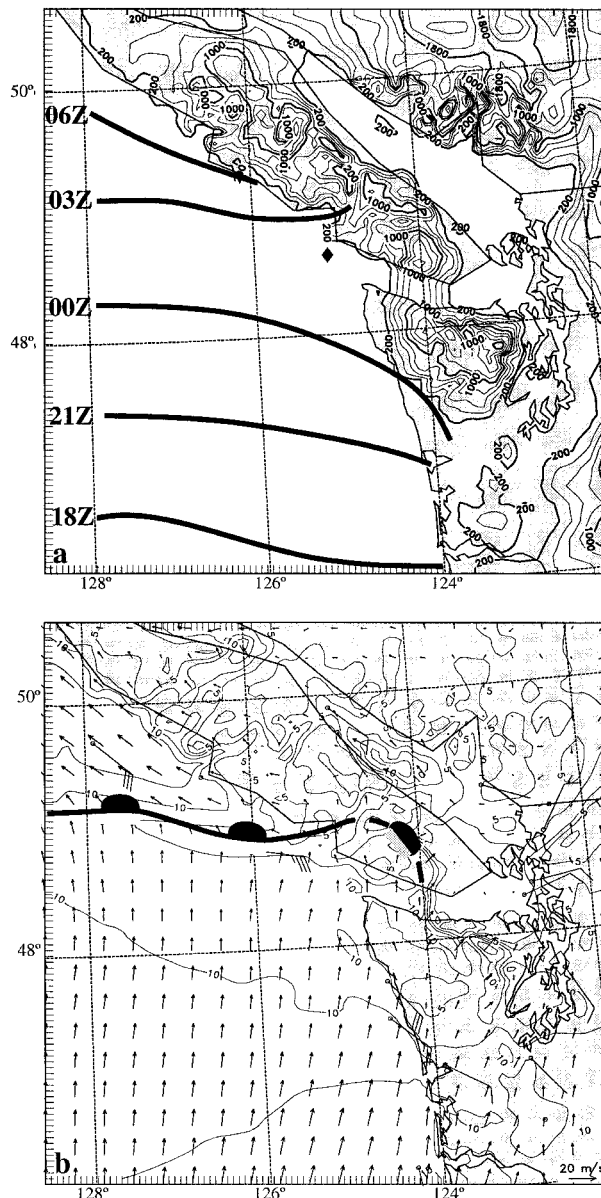


FIG. 27. (a) As in Fig. 26, except for the sensitivity experiment with a barrier near the exit of the Strait of Juan de Fuca.

For example, the upstream flow in the warm sector was characterized by $Fr \sim 1.0$ (as discussed in reference to Fig. 20), which is near the critical value for the onset of flow splitting and topographic blocking, as noted by Smolarkiewicz and Rotunno (1989). It is unclear, however, whether a Froude number, characteristic of the incident flow in the warm sector, solely can be used to diagnose the flow response for the present case. The existence of the cool air trapped along Vancouver Island, with a source from the Strait of Juan de Fuca, and with the associated preexisting along-barrier momentum certainly complicates and perhaps invalidates any simple scale analysis.

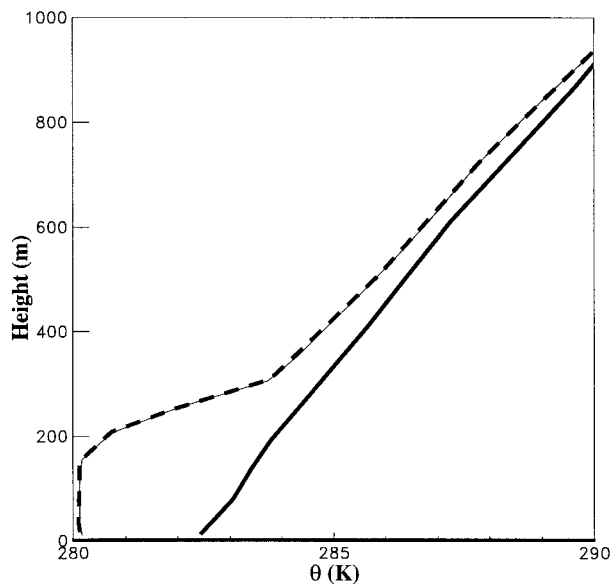


FIG. 28. Vertical profiles of potential temperature valid at 0000 UTC 10 Dec 1995 (24 h) for the control model simulation (dashed line) and simulation with the barrier in the Strait of Juan de Fuca (solid line). The profile location is represented by the diamond in Figs. 6a and 27a.

The effect of low-level easterly flow, which originated from the Strait of Juan de Fuca gap, on the warm frontal movement is illustrated by the 10-m wind field for the simulation with the artificial barrier in the western strait for 0300 UTC 10 December 1995 (Fig. 27b). The results indicate that the low-level warm front is located farther north than either the control (Fig. 19c) or the no-Vancouver Island topography (Fig. 26b) simulations. The surface front isochrones, shown in Fig. 27a, indicate steady northward movement of the warm front when the cold strait outflow is blocked. It can thus be inferred for the control case that the frontal blocking is enhanced due to the increased static stability locally introduced by cold strait outflow. This situation with continental outflow increasing the low-level static stability has been recently shown to enhance frontal blocking in other geographic areas, such as during the California Land-falling Jets Experiment (M. Ralph 2000, personal communication).

Vertical profiles of simulated potential temperature valid at 0000 UTC 10 December 1995 (24 h) for a point upstream of Vancouver Island for the control and barrier-in-strait simulations (location denoted by diamond in Figs. 6a and 27a) are displayed in Fig. 28. The cold air mass trapped upstream of the topography is evident in the control simulation (dashed line) and is absent in the sensitivity experiment with the barrier in the Strait of Juan de Fuca (solid line). The disruption of the low-level easterly flow from the strait, apparent in the sensitivity experiment (Fig. 27), acts to deplete the cold air mass upstream of the Vancouver Island topography, resulting in reduced static stability relative to the control.

Clearly, for a given incident flow, the impact of the greater low-level stability in the control is to decrease Fr , which is consistent with the deceleration of the warm front as it approached the topography relative to the barrier-in-strait sensitivity experiment. Thus, in this case the nearshore easterly flow originating from over the Strait of Juan de Fuca appears to be important for frontal impedance and acts in concert with blocking effects due to the coastal orography.

6. Summary and conclusions

This case represents, to our knowledge, the first detailed depiction of a warm front approaching a coast with prominent terrain. The goal of our analysis has been to document the interactions between this front and a cool, low-level air mass that was situated along the southwest portion of Vancouver Island. Using observations from a P-3 aircraft and high-resolution numerical simulations, we have described mesoscale circulations and precipitation distributions during this event, and characterized the boundary layer turbulence.

The warm front had a classic structure while offshore, including a noticeable but gradual wind shift and temperature change over 20–30 km, a pronounced transition in static stability, and a relatively shallow slope. A band of enhanced precipitation (5–10 dBZ above background) was located in the vicinity of the low-level frontal zone. Some significant changes occurred as the front encountered the cool, trapped flow extending about 100 km offshore of Vancouver Island. Its progress slowed markedly, from about 10 to 3 m s⁻¹. The precipitation band associated with the front while it was offshore appeared to detach from the surface front and advance toward and over Vancouver Island as the front slowed. This aspect is uncertain, however, because of our difficulty both during the flight and in subsequent analysis of the radar data, in distinguishing between propagation and downstream development of the precipitation in the immediate vicinity of Vancouver Island.

The cool air mass trapped along Vancouver Island had a number of important characteristics. It featured strong (~ 25 m s⁻¹) low-level winds oriented parallel to the shore and terrain. This flow was about 700 m deep, with a flat upper boundary, at least within about 70 km of the coast. It extended roughly 100 km offshore because that is approximately the point where the progress of the surface warm front slowed. The transition between the trapped flow from the southeast and the overlying flow from the southwest was concentrated into a thin (~ 100 m) layer with large vertical wind shear and static stability. The lack of a tilt to this trapped flow is a departure from classic barrier jet situation, which generally includes an upslope component (Parish 1982; Bell and Bosart 1988). The surface winds at the coast before frontal landfall (Figs. 4a,b) included a downslope component and little pressure ridging appeared to be occurring along the coast of Vancouver Island. Hence the

geostrophic adjustment in the nearshore, trapped flow was probably minimal [unlike the cold-air damming case studied by Bell and Bosart (1988) and the gap wind case of Lackmann and Overland (1989)]. It is possible that a secondary circulation associated with the front at 2200–2300 UTC (Figs. 10–12) also acted to help level the trapped flow. The trapped flow may be best attributed to the flow of cool, continental air out of the Strait of Juan de Fuca. The characteristics of this trapped flow may therefore be more controlled by boundary layer turbulent and radiative processes in its source region, that is, over the interior Pacific Northwest, than by local orographic effects. It is unclear, however, to what degree the character (e.g., momentum, depth, stability) of the trapped flow impacts the front as it approaches the coastal terrain.

Multiscale numerical simulations of the warm front approaching Vancouver Island using a nonhydrostatic model, COAMPS, illustrate the complex nature of the forcing in the coastal zone. The simulated vertical structure of the warm front was in reasonable agreement with the aircraft observations; however, the trapped flow depth was ~ 200 m too shallow. The most notable model error was that the low-level jet was $5\text{--}10\text{ m s}^{-1}$ too weak, which is consistent with the shallower cold air mass. Frontogenesis was enhanced due to the superposition of the warm frontal baroclinic zone and the cold-air outflow from the Strait of Juan de Fuca.

As the warm front approached the coast, the model-simulated movement slowed significantly from an average speed of 8 m s^{-1} between 1800 UTC 9 December and 0000 UTC 10 December to less than 3 m s^{-1} between 0300 and 0600 UTC 10 December. The upstream Fr was approximately unity, which is near the threshold for three-dimensional blocking. Sensitivity experiments suggested that the frontal blocking occurred primarily as a result of the shallow cold easterly flow that exited the Strait of Juan de Fuca and was further enhanced by the steep orography of Vancouver Island. The simulation results underscore the difficulty of applying conventional scaling parameters, established in previous theoretical studies, to a complex three-dimensional flow situation that contains a cold-air source along the upstream portion of the coastal topography. Low-level accelerations in the easterly flow located just downstream of the Strait of Juan de Fuca exit were apparent in both the research aircraft observations and highest-resolution ($\Delta x = 1.67\text{ km}$) nested grid results. The model simulation exhibited transcritical expansion fan characteristics due to the lateral flow divergence consistent with the wind speed maximum.

Some details about the character of the boundary layer turbulence during this case were examined using mean and fast-response flight-level measurements. Our emphasis during this flight was the collection of Doppler radar measurements and so we were unable to map turbulent structures with the kind of detail that has been done before, notably by Berger and Friehe (1995) for

the warm sector of an Experiment on Rapidly Intensifying Cyclones over the Atlantic storm. Nevertheless, we did find some substantial differences in the magnitude and nature of the turbulence between the warm sector, frontal zone, and trapped flow regions. The most interesting of these differences is between the turbulence in the frontal zone and that in the trapped flow regions, even though the mean winds were similar. The frontal zone had much greater quadrature between the cross-wind component and the vertical velocity, and much greater momentum fluxes in the cross-wind component than was found in the nearshore region of trapped flow. The momentum fluxes were likely due to the breakdown of the gravity waves that were responsible for the quadrature involving the cross-wind component. The nearshore region featured the highest values found for the along-wind momentum fluxes and TKE; here the turbulence maybe associated predominantly with buoyancy and shear production in the surface layer. The turbulent characteristics of the warm front and trapped flow were simulated realistically. For example, the primary TKE maximum occurred in the trapped flow near the shore of Vancouver Island and was predominantly forced by shear production of the coast parallel wind component with secondary buoyancy generation due to the cold easterly flow overlying the warmer sea surface. A secondary TKE maximum, positioned along sloping warm frontal zone, was forced by shear production, which dominated the damping effects of buoyancy associated with the frontal inversion. The simulated TKE in the warm sector was significantly weaker than the research aircraft observations indicated.

We conclude by noting that while this case bears some resemblance to that of Overland and Bond (1995), for example, both are characterized by incident flow from the southwest and an internal Fr of approximately unity, the present case also features significant time-dependent and diabatic effects. The simple scaling used by Overland and Bond (1995) is therefore not expected to be as meaningful. Instead, the evolution and progress of the surface front in the immediate vicinity of Vancouver Island was controlled by a more complex interplay between the cool air flowing out of the strait, the mixing between this air mass and the overlying warm sector flow, and low-level pressure changes imposed from aloft, as well as the direct effects of the orography.

Acknowledgments. The authors wish to recognize the assistance of Drs. Brad Smull and Cheng-Ku Yu in the processing of the Doppler radar data, and Drs. Carl Friehe and Bernie Walter in the processing of the turbulence data. The research support for the first author was provided by the Office of Naval Research (ONR) Program Element 0601153N. The support for the second author was provided ONR under Contract N00014-96-F-0009. Computing time was supported in part by a grant of HPC time from the Department of Defense Shared Resource Center, Stennis Space Center, Mississippi, and

performed on a Cray T-90. This publication represents Contribution 718 by the Joint Institute for the Study of the Atmosphere and Ocean (JISAO) and Contribution 2132 by the Pacific Marine Environmental Laboratory (PMEL). Comments from the anonymous reviewers significantly improved the manuscript.

REFERENCES

- Bell, G. D., and L. F. Bosart, 1988: Appalachian cold-air damming. *Mon. Wea. Rev.*, **116**, 137–161.
- Berger, B. W., and C. A. Friehe, 1995: Boundary-layer structure near the cold front of a marine cyclone during ERICA. *Bound.-Layer Meteor.*, **73**, 227–253.
- Bjerknes, J., and H. Solberg, 1921: Meteorological conditions for the formation of rain. *Geophys. Publ.*, **2** (3), 1–60.
- Blumen, W., and B. Gross, 1987: Advection of a passive scalar over a finite-amplitude ridge in a stratified rotating atmosphere. *J. Atmos. Sci.*, **44**, 1696–1705.
- Bond, N., and Coauthors, 1997: The Coastal Observation and Simulation with Topography (COAST) experiment. *Bull. Amer. Meteor. Soc.*, **78**, 1941–1955.
- Braun, S. A., R. A. Houze, and B. F. Smull, 1997: Airborne dual-Doppler observations of an intense frontal system approaching the Pacific Northwest coast. *Mon. Wea. Rev.*, **125**, 3131–3156.
- , R. Rotunno, and J. B. Klemp, 1999: Effects of coastal orography on landfalling cold fronts. Part I: Dry, inviscid dynamics. *J. Atmos. Sci.*, **56**, 517–533.
- Brost, R. A., J. C. Wyngaard, and D. H. Lenschow, 1982: Marine stratocumulus layers. Part II: Turbulence budgets. *J. Atmos. Sci.*, **39**, 818–836.
- Browning, K. A., and T. W. Harrold, 1970: Air motion and precipitation growth at a cold front. *Quart. J. Roy. Meteor. Soc.*, **96**, 369–389.
- Colle, B. A., and C. F. Mass, 1996: An observational and modeling study of the interaction of low-level southwesterly flow with the Olympic Mountains during COAST IOP 4. *Mon. Wea. Rev.*, **124**, 2152–2175.
- , and —, 2000: High resolution observations and numerical simulations of gap flow through the Strait of Juan de Fuca on 9–10 December 1995. *Mon. Wea. Rev.*, **128**, 2393–2422.
- , —, and B. F. Smull, 1999: An observational and numerical study of a cold front interacting with the Olympic Mountains during COAST IOP 5. *Mon. Wea. Rev.*, **127**, 1310–1334.
- Davies, H. C., 1976: A lateral boundary formulation for multi-level prediction models. *Quart. J. Roy. Meteor. Soc.*, **102**, 405–418.
- , 1984: On the orographic retardation of a cold front. *Beitr. Phys. Atmos.*, **57**, 409–418.
- Doyle, J. D., and T. T. Warner, 1990: Mesoscale coastal processes during GALE IOP 2. *Mon. Wea. Rev.*, **118**, 283–308.
- , and M. A. Shapiro, 2000: A multi-scale simulation of an extreme downslope windstorm over complex topography. *Meteor. Atmos. Phys.*, **74**, 83–101.
- Durrán, D. R., and J. B. Klemp, 1983: A compressible model for the simulation of moist mountain waves. *Mon. Wea. Rev.*, **111**, 2341–2361.
- Gal-Chen, T., and R. C. J. Somerville, 1975: On the use of a coordinate transformation for the solution of the Navier–Stokes equations. *J. Comput. Phys.*, **17**, 209–228.
- Gross, B. D., 1994: Frontal interaction with isolated orography. *J. Atmos. Sci.*, **51**, 1480–1496.
- Grønås, S., 1995: The seclusion intensification of the New Year day storm 1992. *Tellus*, **47**, 733–746.
- Harshvardhan, R., Davies, D., Randall, and T. Corsetti, 1987: A fast radiation parameterization for atmospheric circulation models. *J. Geophys. Res.*, **92**, 1009–1015.
- Hertzman, O., P. V. Hobbs, and J. D. Locatelli, 1988: The mesoscale and microscale organization of clouds and precipitation in mid-latitude cyclones. XVI: Three-dimensional airflow and vertical vorticity budget for a warm front. *J. Atmos. Sci.*, **45**, 3650–3666.
- Heymsfield, G. M., 1979: Doppler radar study of a warm frontal region. *J. Atmos. Sci.*, **36**, 2093–2107.
- Hodur, R. M., 1997: The Naval Research Laboratory's Coupled Ocean/Atmosphere Mesoscale Prediction System (COAMPS). *Mon. Wea. Rev.*, **125**, 1414–1430.
- Hogan, T. F., and T. E. Rosmond, 1991: The description of the U.S. Navy Operational Global Atmospheric Prediction System's spectral forecast model. *Mon. Wea. Rev.*, **119**, 1786–1815.
- Kain, J. S., and J. M. Fritsch, 1993: Convective parameterization for mesoscale models: The Kain-Fritsch scheme. *The Representation of Cumulus Convection in Numerical Models*, Meteor. Monogr., No. 46, Amer. Meteor. Soc., 165–170.
- Khelif, D., S. P. Burns, and C. A. Friehe, 1999: Improved wind measurements on research aircraft. *J. Atmos. Oceanic Technol.*, **16**, 860–875.
- Klemp, J., and R. Wilhelmson, 1978: The simulation of three-dimensional convective storm dynamics. *J. Atmos. Sci.*, **35**, 1070–1096.
- Lackmann, G. M., and J. E. Overland, 1989: Atmospheric structure and momentum balance during a gap-wind event in Shelikof Strait, Alaska. *Mon. Wea. Rev.*, **117**, 1817–1833.
- Locatelli, J. D., and P. V. Hobbs, 1987: The mesoscale and microscale organization of clouds and precipitation in midlatitude cyclones. XIII: Structure of a warm front. *J. Atmos. Sci.*, **44**, 2290–2309.
- Louis, J. F., 1979: A parametric model of vertical eddy fluxes in the atmosphere. *Bound.-Layer Meteor.*, **17**, 187–202.
- Mellor, G. L., and T. Yamada, 1982: Development of a turbulence closure for geophysical fluid problems. *Rev. Geophys. Space Phys.*, **20**, 851–875.
- Metcalf, J. I., 1975: Gravity waves in a low-level inversion. *J. Atmos. Sci.*, **32**, 351–361.
- Neiman, P. J., M. A. Shapiro, and L. S. Fedor, 1993: The life cycle of an extratropical marine cyclone. Part II: Mesoscale structure and diagnostics. *Mon. Wea. Rev.*, **121**, 2177–2199.
- Overland, J. E., and N. Bond, 1993: The influence of coastal orography: The Yakutat storm. *Mon. Wea. Rev.*, **121**, 1388–1397.
- , and —, 1995: Observations and scale analysis of coastal wind jets. *Mon. Wea. Rev.*, **123**, 2934–2941.
- Parish, T. R., 1982: Barrier winds along the Sierra Nevada mountains. *J. Appl. Meteor.*, **21**, 925–930.
- Parsons, D. B., and P. V. Hobbs, 1983: The mesoscale and microscale structure and organization of clouds and precipitation in mid-latitude cyclones. IX: Some effects of orography on rainbands. *J. Atmos. Sci.*, **40**, 1930–1949.
- Pierrehumbert, R. T., and B. Wyman, 1985: Upstream effects of mesoscale mountains. *J. Atmos. Sci.*, **42**, 977–1003.
- Rogers, D. P., 1995: Coastal meteorology. *Rev. Geophys.*, **33**, 880–895.
- Rotunno, R. J., and Coauthors, 1992: *Coastal Meteorology, A Review of the State of the Science*. National Academy Press, 99 pp.
- Rutledge, S. A., and P. V. Hobbs, 1983: The mesoscale and microscale structure of organization of clouds and precipitation in midlatitude cyclones. VIII: A model for the “seeder-feeder” process in warm-frontal rainbands. *J. Atmos. Sci.*, **40**, 1185–1206.
- Schär, C., and D. R. Durrán, 1997: Vortex formation and vortex shedding in continuously stratified flow past isolated topography. *J. Atmos. Sci.*, **54**, 534–554.
- Schumann, U., 1987: Influence of mesoscale orography on idealized cold fronts. *J. Atmos. Sci.*, **44**, 3423–3441.
- Smith, R. B., 1979: The influence of mountains on the atmosphere. *Advances in Geophysics*, Vol. 21, Academic Press, 87–230.
- , 1989: Hydrostatic flow over mountains. *Advances in Geophysics*, Vol. 31, Academic Press, 1–41.
- Smolarkiewicz, P. K., and R. Rotunno, 1989: Low Froude number flow past three-dimensional obstacles. Part I: Baroclinically generated lee vortices. *J. Atmos. Sci.*, **46**, 1154–1164.
- Steenburgh, W. J., and C. F. Mass, 1996: Interaction of an intense

- extratropical cyclone with coastal orography. *Mon. Wea. Rev.*, **124**, 1329–1352.
- Therry, G., and P. LaCarrère, 1983: Improving the eddy kinetic energy model for planetary boundary layer description. *Bound.-Layer Meteor.*, **25**, 63–88.
- Volkert, H. L., L. Weickman, and A. Tafferger, 1991: The “Papal Front” of 3 May 1987—A remarkable example of frontogenesis near the Alps. *Quart. J. Roy. Meteor. Soc.*, **117**, 125–150.
- Wakimoto, R. M., W. Blier, and C. Liu, 1992: On the frontal structure of an explosive oceanic cyclone. *Mon. Wea. Rev.*, **120**, 1135–1155.
- Williams, R. T., M. S. Peng, and D. A. Zankofsi, 1992: Effects of topography on fronts. *J. Atmos. Sci.*, **49**, 287–305.
- Yu, C.-K., and B. F. Smull, 2000: Airborne Doppler observations of a landfalling cold front upstream of steep coastal orography. *Mon. Wea. Rev.*, **128**, 1577–1603.